INVESTIGATION OF A GRAVITY WAVE DUCTING EVENT IN THE UPPER MESOSPHERE

BY

ANTHONY C. CATON

THESIS

Submitted in partial fulfillment of the requirements
for the degree of Master of Science in Electrical and Computer Engineering
in the Graduate College of the
University of Illinois at Urbana-Champaign, 2019

Urbana, Illinois

Adviser:

Professor Emeritus Gary R. Swenson

Abstract

Atmospheric gravity waves (GWs) play an important role in the transport of energy and momentum throughout the Earth's atmosphere. GW effects couple the lower regions of the atmosphere with the middle and upper regions of the atmosphere and the neutral atmosphere with the ionosphere. The effects are particularly strong in the mesosphere and lower thermosphere (MLT), where upward-propagating GWs tend to deposit momentum and energy flux via breaking, viscous dissipation, or other processes. The resulting net drag, heating, and cooling impact the global circulation of the mean atmospheric flow. Consequently, the parameterization of GWs in global climate models is a key focus of contemporary research on the MLT region. The physical processes associated with GWs must be understood in addition to their statistical characteristics in order to better parameterize their effects on the atmosphere. Ducting is a process that can occur when a GW becomes trapped between two evanescent regions in the atmosphere. According to the linear GW theory, a fully ducted wave has zero vertical momentum flux, so the ducting process must also be understood in order to improve our parameterization of GWs in global climate models. In this thesis, correlative lidar and airglow observations of a highly resonant ducting event, which occurred on the night of January 18, 2015, above the Andes Lidar Observatory (ALO) on Cerro Pachón, Chile (30.0° S, 70.0° W), are presented and analyzed. A ducted quasi-monochromatic GW with large associated temperature (T') and vertical wind (w') perturbations was observed in the mesopause region. A coherent phase relationship, consistent with the linear GW theory, between the temperature and vertical wind perturbations associated with the GW was found. The results also appear to show the generation of a secondary upward-propagating wave above the primary duct.

Acknowledgments

I would like to thank my adviser, Dr. Gary R. Swenson, for his wisdom and guidance in my graduate career. I would not be where I am today without his willingness and enthusiasm to introduce me to the field of remote sensing and space science. I would also like to thank Dr. Fabio Vargas for his willingness to share advice, code snippets, and other support which have directly led to the improvement of this thesis. I also acknowledge Dr. Alan Z. Liu, whose work in processing and uploading the publicly available lidar data on the ALO website (http://lidar.erau.edu/data/nalidar/index.php) has been greatly appreciated.

I greatly appreciate the friendship and comradery that all the graduate students in the Remote Sensing/Space Science area at UIUC, including Channing Philbrick, Nicholas Ratajczyk, Kristina Chu, Matthew Grawe, Zipeng Wang, Yamuna Phal, and many others, have provided me over the last two years. I will always cherish the memories made with you all at CEDAR and on campus.

Lastly, I would like to thank all my family and friends for the immeasurable support they have provided over the years. Special thanks go out to my immediate family: my mother Anne Caton, my father John Caton, my sister Caroline Caton, and my brother Dana Caton. I would also like to thank my whole extended family, especially my cousin David Mast and my grandmother Phyllis Mast, as well as my uncle and aunt Dan & Laura Mast for introducing me to Dr. Swenson, allowing me the opportunity to live on their property at a discounted rate, and other support. I love and appreciate you all.

This work has been supported by the NSF Geosciences Division under the Grant AGS 11-36208.

Table of Contents

1. Introduction

1.1 Background

The mesosphere and lower thermosphere (MLT), which together constitute a significant part of the middle region of Earth's atmosphere, lie above the uppermost vertical reaches of aircraft or common radiosondes and below the orbital altitude of satellites. Consequently, observations of the MLT region of the atmosphere rely primarily on remote sensing techniques or in-situ measurements by rocket-borne instruments. These measurements generally have limited temporal or spatial breadth, and as a result, the MLT region is one of the least understood regions of Earth's atmosphere. The mesopause region at roughly 85–100 km [Xu et al., 2007] is of contemporary interest because it serves as a transition region between the neutral atmosphere and the ionosphere.

In general, the Earth's atmosphere is a stably stratified fluid in which wave motion is supported [Nappo, 2012]. A vertically perturbed parcel of fluid in the Earth's atmosphere will have restorative forces acting on it due to the Earth's gravitational field and buoyancy arising from the negative atmospheric density gradient with altitude. The resulting oscillation, known as a gravity wave (GW), can propagate through the atmosphere. In the mesopause region, upward-propagating GWs have been observed to deposit significant momentum and energy to the mean flow by several different mechanisms, including dissipation and breaking induced by wave interactions with the mean flow [Fritts and Rastogi, 1985; Franke and Robinson, 1999] and viscous dissipation at higher altitudes in the lower thermosphere [Liu et al., 2013]. The momentum and energy fluxes associated with GWs have been observed to profoundly influence the atmosphere on a global scale. For example, GWs are an important driver of the Brewer-Dobson circulation of meridional winds [Cohen et al., 2014] and the quasi-biennial and semi-annual oscillations of stratospheric zonal winds [Ern et al., 2014; Ern et al., 2015]. Wave-induced diffusion and

energy flux affect the vertical transport of atmospheric constituents such as atomic oxygen (O), meteoric iron (Fe), and meteoric sodium (Na) in the mesopause region [Gardner, 2018]. GWs also influence processes which occur on smaller scales, such as turbulent mixing and the formation of instabilities [Liu et al., 2004; Guo et al., 2017; Fritts et al., 2013]. Atmospheric GWs are typically generated in the lower atmosphere and propagate upwards, though a relatively small fraction of GWs propagate downwards [Shimizu and Tsuda, 1997]. In the lower atmosphere, the primary GW generation mechanisms are orography, convection, and geostrophic adjustment [Fritts and Alexander, 2003, and references therein]. Model studies have shown that GW breaking can generate secondary waves [Vadas et al., 2003; Liu et al., 1999] and observations have been made in the MLT that suggest the occurrence of secondary wave generation through wave breaking [Vargas et al., 2016; Bossert et al., 2017]. The transfer of energy and momentum associated with all of these GW processes couples the lower atmosphere with the middle and upper atmosphere. Furthermore, the thermal balance of the middle atmosphere is altered by GW momentum and energy flux such that the equilibrium state is dynamical, rather than radiative [Gierasch et al., 1970; Andrews et al., 1987; Liou, 2002]. Therefore, we must understand the generation and dissipation mechanisms and propagation characteristics of GWs in order to better understand the weather and climate of the whole atmosphere.

An abundance of atmospheric waves including GWs, planetary waves, and tides are present in the MLT region. The interactions between waves, the mean flow, and other waves complicate the dynamical processes which couple the MLT and other atmospheric regions. In order to study these processes, we must make temporally and spatially resolved measurements of atmospheric properties such as temperature, density, and wind speed vectors. Fortunately, the MLT region contains metal and airglow layers which can be used to measure atmospheric properties by remote sensing methods [Khomich et al., 2008]. Two particularly useful airglow sources are the hydroxyl (OH) Meinel band emission, which emits over a wide spectral range (0.7–4.0 μm), and the neutral atomic oxygen (OI) visible green line (557.7 nm).

The OH and OI airglow emissions will be discussed in more detail in Section 2.1.2. A persistent global sodium layer also exists near an altitude of 92 km, which is produced primarily by the ablation of dust entering Earth's atmosphere from the interplanetary medium [Plane et al., 2015]. The Na layer has been used extensively to measure temperature and wind velocities in the mesopause region through resonance-fluorescence lidar observations at the 589.158 nm Na D_{2a} transition [e.g., Bossert et al., 2014; Guo et al., 2017]. The resonance-fluorescence lidar technique will be discussed in more detail in Section 2.1.1.

1.2 Linear Gravity Wave Theory

1.2.1 Development of the Linear Gravity Wave Theory

The linear theory of gravity waves is the basis for many theoretical studies of propagating GWs. Consider a set of fundamental variables

$$q = (p, \rho, u, v, w), \tag{1.1}$$

where p, ρ, u, v, and w are the pressure, density, zonal wind, meridional wind, and vertical wind respectively. In general, GWs are governed by the Euler equations for the set q. Under the linear theory, we can expand each variable q into the sum of a background state $\bar{q}$ and a small perturbation q'. We may assume that the background state is steady or sufficiently slowly varying and horizontally uniform, with variations only in the vertical direction. We also assume that q' is independent of $\bar{q}$ and much smaller than $\bar{q}$. The process of linearizing the Euler equations from this point depends on what further assumptions are made, but the result is a standard wave equation in the vertical direction of the form

$$\frac{d^2\phi(z)}{dz^2} + m^2\phi(z) = 0. \tag{1.2}$$

The GW dispersion relation relates the vertical wavenumber *m* to the horizontal wavenumber *k* and the background state $\bar{q}$. The full GW dispersion relation is derived from the 3-D Euler equations for a compressible and irrotational atmosphere in the presence of vertically varying temperature and winds and is shown as equation (9) of Zhou and Morton [2007].

A particularly useful form of the 2-D Euler equation under the Boussinesq approximation in an isothermal and continuous shear flow was derived independently by Taylor [1931] and Goldstein [1931]. The equation, known as the Taylor-Goldstein equation [Nappo, 2012], can be used (see Appendix B) to derive a reduced form of the GW dispersion relation:

$$m^2 = \frac{N^2}{(c-\bar{u})^2} - k^2 - \frac{1}{4H_s^2} + \frac{1}{(c-\bar{u})}\frac{d^2\bar{u}}{dz^2} - \frac{1}{H_s(c-\bar{u})}\frac{d\bar{u}}{dz}, \tag{1.3}$$

where N^2 is the squared buoyancy frequency, H_s is the pressure scale height of the atmosphere, *c* is the observed horizontal phase speed, $\bar{u}$ is the background wind speed in the direction of wave propagation, and the quantity $(c-\bar{u})$ is the intrinsic horizontal phase speed of the wave. If the last two terms of Equation (1.3) relating to wind shear are ignored, then the dispersion relation reduces to the form originally derived by Hines [1960]

$$m^2 = \frac{N^2}{(c-\bar{u})^2} - k^2 - \frac{1}{4H_s^2}. \tag{1.4}$$

The solution to Equation (1.2) for $m^2 > 0$ has the form $\phi(z) = Ae^{imz}$, in which the amplitude of ϕ has a sinusoidal variation in altitude with vertical wavelength $\lambda_z = \frac{2\pi}{m}$. Such waves are known as propagating or internal waves. For the opposite case of $m^2 < 0$, i.e., $m = i\tilde{m}_{Im}$, the form of the solution is the decaying exponential $\phi(z) = Ae^{-i\tilde{m}_{Im}z}$. The coefficient *A* is an arbitrary amplitude. The amplitude of such waves decays exponentially with altitude and they are referred to as evanescent or external waves. It is clear from Equation (1.3) that the value of m^2 is dependent on the intrinsic horizontal phase

speed of the wave and the background atmosphere. The solutions to Equation (1.2) require that m is independent of altitude, which is generally not the case since the background temperature and winds typically vary with altitude. The solutions are still valid if we apply the Wentzel-Kramers-Brillouin (WKB) approximation that the background temperature and winds vary slowly within a vertical wavelength.

The dispersion relation (1.3) can be used to characterize the capability of a measured or parameterized vertical atmospheric profile to support wave propagation. Evanescent regions can cause partial or total reflection of GWs. Two parallel horizontal evanescent layers can therefore confine the propagation of a GW. This process is known as ducting and will be discussed in more detail in Section 1.2.2. Furthermore, when a GW propagates to an altitude where the horizontal phase speed of the wave matches the background wind speed in the wave propagation direction (i.e., $(c - \bar{u}) = 0$), the intrinsic frequency of the wave goes to zero and the wave will break and transfer momentum to the background atmosphere. This process, which occurs continually in the MLT region, is known as critical-layer filtering [Fritts and Alexander, 2003].

Polarization relations that relate the phase and amplitude of various wave quantities can also be derived from the linearized wave equations. For example, it can be shown [e.g., Vadas, 2013] that the polarization relation between the complex wave amplitudes of the relative temperature perturbation $\hat{T} = \frac{T'}{\bar{T}}$ and the vertical wind perturbation $\hat{w}$ is given by

$$\frac{\hat{T}}{\hat{w}} = \frac{N^2\left(im + \frac{1}{2H_s}\right) - \frac{\hat{\omega}^2}{\gamma H_s}(\gamma - 1)}{g\hat{\omega}\left(-m - \frac{i}{2H_s} + \frac{i}{\gamma H_s}\right)}, \tag{1.5}$$

where $\hat{\omega}$ is the intrinsic wave frequency and $\gamma \approx 1.4$ is the ratio of the specific heats at constant pressure and volume, whose values are given in Table 1.1. In the Boussinesq limit, Equation (1.5) reduces to

$$\frac{\hat{T}}{\hat{w}} = \frac{iN^2}{g\hat{\omega}}. \tag{1.6}$$

The polarization relation (1.6) indicates that for an internal GW, the temperature and vertical wind perturbations are out of phase by 90°. In general, a significant deviation in observed phases or amplitudes from the theoretical predictions of the polarization relations indicates wave dissipation, or saturation.

Table 1.1: Physical parameters and constants used in this thesis, specified for the neutral atmosphere in the 85–110 km altitude range.

Variable	Name	Value
c_p	Specific heat at constant pressure	1004 $JK^{-1}kg^{-1}$
c_v	Specific heat at constant volume	717 $JK^{-1}kg^{-1}$
R	Ideal gas constant for a dry atmosphere	287 $JK^{-1}kg^{-1}$
R_E	Radius of Earth	6371 km
G	Gravitational constant	6.67408×10^{-11} $m^3kg^{-1}s^{-2}$
M_E	Mass of Earth	5.972×10^{24} kg
$g = \frac{GM_E}{(R_E + z)^2}$	Gravitational acceleration	≈9.5 ms^{-2}
$H_s = \frac{R\bar{T}}{g}$	Pressure scale height	~6 km

1.2.2 Gravity Wave Ducting

Internal gravity waves between evanescent layers in the MLT can become vertically trapped with sustained horizontal propagation. Two distinct ducting mechanisms, thermal ducts and Doppler ducts, have been identified [e.g., Friedman, 1966; Chimonas and Hines, 1986]. Thermal ducts are layers in which a wave becomes trapped due to variations of the buoyancy frequency *N* in the background atmosphere. The squared buoyancy frequency can be written as

$$N^2 = \frac{g}{T}\left(\frac{dT}{dz} + \frac{g}{c_p}\right), \tag{1.7}$$

where T is the temperature of the background atmosphere and the quantity $g/c_p \approx 9.5$ K km^{-1} is the dry adiabatic lapse rate. Regions where N^2 is less than zero, i.e., the negative temperature gradient is larger than the dry adiabatic lapse rate, are indicative of static or convective instability. Consideration of Equation (1.7) in the simplified dispersion relation (1.4) indicates that a temperature inversion inside a region with an otherwise negative temperature gradient can potentially be a thermal duct. Since the mesopause region is the coldest part of the atmosphere, temperature inversions that form in this region can therefore be thermal ducts. Likewise, analysis of the dispersion relation (1.3) suggests that ducting can also occur in regions where there exists a distinct maximum or minimum in the horizontal winds. This type of ducting is called Doppler ducting and occurs independently of thermal ducting. The effects of Doppler ducting are maximized when the horizontal winds are along the direction of wave propagation [Chimonas and Hines, 1986]. Numerical simulations also indicate that thermal and Doppler ducting can occur simultaneously in the mesopause region [Walterscheid and Hickey, 2009].

A fully ducted wave, or a wave which propagates along the duct with no loss of energy, is necessarily a resonant wave which satisfies the kinematic and dynamic continuity conditions at the boundaries of the duct. Waves which do not match the resonance conditions of the duct cannot freely propagate along the duct and will decay in the absence of external forcing. In order to understand the basic mechanism behind the ducting process, we may consider a simplified three-layer model with constant m in each layer. In the middle layer, denoted layer 2, we set $m^2 > 0$, and in the two surrounding layers, denoted layers 1 and 3, we set $m^2 < 0$. For a model atmosphere with constant horizontal winds and temperature in each layer, then the vertical wavenumber m_k is constant within each layer k = 1, 2, 3. If we set z = 0 as the center of the inversion, the solution of Equation (1.2) in layer 2 has the form

$$\phi_2(z) = A_2 e^{im_2 z} + B_2 e^{-im_2 z}, \tag{1.8}$$

and in layers 1 and 3 it has the form

$$\phi_k(z) = A_k e^{\pm \tilde{m}_k z} \quad (k = 1, 3), \tag{1.9}$$

where $\tilde{m}_k i^2 = -m_k^2$. The plus sign in Equation (1.9) applies in layer 1 and the minus sign applies in layer 3. The forms of the solutions in Equation (1.9) ensure that the vertically integrated kinetic energy density remains finite. We may obtain a characteristic equation by subjecting Equations (1.8) and (1.9) to the kinematic and dynamic continuity conditions at the interfaces between layers. The equation must be numerically solved for its eigenvalues for a given middle layer thickness *D*, wave horizontal phase speed, and horizontal wind speed in the middle layer, but the eigenfunctions which satisfy the boundary and continuity conditions have the form [Walterscheid and Hickey, 2009]

$$\phi_2(z) = A\left(\cos\left[m_2\left(z + \frac{D}{2}\right)\right] + \tilde{K}_{12}\sin\left[m_2\left(z + \frac{D}{2}\right)\right]\right) \tag{1.10}$$

in the middle layer, and

$$\phi_k(z) = Ae^{\left[-\tilde{m}_k\left(z \pm \frac{D}{2}\right)\right]} \quad (k = 1, 3) \tag{1.11}$$

in layers 1 and 3, where *A* is an arbitrary amplification factor. In Equation (1.8), $\tilde{K}_{12}$ is a complex coefficient related to the value of m_1 and m_2, the choices of horizontal wind speeds in layers 1 and 2, and the horizontal phase speed of the wave. In Equation (1.11), the sign convention is the same as in Equation (1.9). For an internal GW, we can assume a general 2-D waveform solution of the form

$$\Phi(x, z) = \phi_k(z)\bar{\rho}^{-\frac{1}{2}} e^{i(kx - \omega t)} \quad (k = 1, 2, 3), \tag{1.12}$$

where x and z are, respectively, the horizontal and vertical coordinates, $\bar{\rho}$ is the mean basic-state density, and t is time. Equation (1.12) indicates that a fully ducted wave propagates horizontally in the middle layer with no leakage of wave energy from the duct.

The three-layer model is an idealized case that does not allow for partially ducted waves, or waves which propagate along the duct while leaking wave energy into the surrounding layers. A full-wave model [e.g., Walterscheid and Hickey, 2009] which numerically solves the coupled second-order differential (Navier-Stokes) continuity equations is required to describe the propagation of GWs through a more realistic atmosphere. Walterscheid and Hickey [2009] implemented the full wave model for a viscous atmosphere with temperature and mean wind profiles which contain altitude variations. The model was run using modified versions of two climatological models, the Mass Spectrometer Incoherent Scatter (MSIS) model [Hedin, 1991] and Horizontal Wind Model (HWM) [Hedin et al., 1996], which were modified to include the presence of a mesospheric temperature inversion (INV) and/or lower thermospheric duct (LTD). The modified runs were compared to reference runs which used unmodified versions of the climatological models. Some of the runs also included modifications to the atmospheric profiles based on conditions present during the GW ducting events observed by Smith et al. [2003, 2005]. The results of the simulations show that the amplification factors A relative to the reference runs are increased, sometimes significantly, for certain wave modes when the INV, LTD, and horizontal wind gradients, or combinations thereof, are present. This indicates that both thermal and Doppler ducting can occur simultaneously if the horizontal wavelength and phase speed of the wave have values falling in ranges which depend on the state of the background atmosphere. Furthermore, the results also indicate that the upward extensions of waves ducted in the INV can propagate up to and become ducted in the LTD, which is always present in the lower thermosphere due to the mean temperature structure with altitude in the MLT.

1.2.3 Gravity Wave Observations and Parameterization

Contemporary GW research can generally be divided into two distinct but related categories. The first category is research which seeks to further our understanding of GW generation, dissipation, and propagation processes. The second is research which aims to develop parameterizations which represent the physical effects of GWs in the atmosphere in order to improve global climate models such as the Whole Atmosphere Community Climate Model (WACCM) [Liu et al., 2018]. A great deal of progress on both perspectives has been made in the last few decades. Scientists have published significant results in observational, theoretical, and numerical studies.

Numerous techniques for in-situ and remote measurements have been or are currently used to observe the effects and characteristics of gravity waves in the MLT and other regions of the atmosphere. In general, all observation techniques excel in some respects and fall short in others. For example, while rocket-borne instruments can make high-resolution measurements in the MLT and other atmospheric regions, the cost of each mission is relatively high, and measurements are limited to very short temporal scales. Active ground-based remote sensing instruments such as lidars or radars have good temporal coverage, but they can only resolve vertical structures. Similarly, passive remote sensing instruments such as ground-based or satellite-based airglow imagers have the best temporal coverage, but stationary imagers can only resolve horizontal structures and satellites are typically limited to observations of waves within a limited range of vertical wavelengths [Fritts and Alexander, 2003]. The GW polarization and dispersion relations may be used in some cases to estimate missing horizontal or vertical information [e.g., Hu et al., 2002; Lu et al., 2015]. However, in order to obtain the most accurate estimates of wave propagation and dissipation characteristics, we must observe GWs in 3-D space. In practice, the 3-D structure of GWs is usually measured with correlative observations from two or more complementary instruments.

Correlative measurements from lidar and airglow imagers are commonly used to study GWs in the MLT [e.g., Hu et al., 2002; Swenson et al., 2003; Bossert et al., 2014]. Lidar measurements provide vertical profiles of temperature and vertical, zonal, and meridional winds at a single location at high resolution, but the horizontal structure of a wave generally cannot be resolved by lidar observations alone. However, airglow imagers can passively capture 2-D vertically integrated images of airglow emission. Since most airglow layers within the MLT have full width at half maximum (FWHM) thicknesses of around 6-10 km [Khomich et al., 2008], airglow imagers only resolve horizontal information in a small vertical layer of MLT. A complementary set of observations from a collocated lidar and airglow imager can therefore be used to investigate the 3-D structure and properties of GWs in the MLT.

It is important to understand the transport of momentum and heat throughout the atmosphere by GW propagation and dissipation in order to better parameterize GW effects in global climate models. The vertical momentum flux $\vec{F}_m$ and vertical heat flux F_{heat} by a GW are proportional to the covariances of the GW vertical wind perturbation *w'* with itself and with *u'*, *v'*, and *T'* [Cao, 2017]:

$$\begin{aligned} \vec{F}_m &= -\bar{\rho}(\overline{u'w'}, \overline{v'w'}, \overline{w'w'}) \\ F_{heat} &= -\bar{\rho}\overline{w'T'}. \end{aligned} \tag{1.13}$$

In Equation (1.13), *u'*, *v'*, and *T'* are the GW perturbations to the zonal wind, meridional wind, and temperature, respectively. The time-dependent drag and cooling or heating constitute the GW effects on the mean flow and are defined, respectively, as the divergence of the momentum and heat fluxes [Fritts and Alexander, 2003; Walterscheid, 1981]:

$$\begin{aligned} \left(\frac{d\bar{u}}{dt}, \frac{d\bar{v}}{dt}, \frac{d\bar{w}}{dt}\right) &= -\frac{1}{\bar{\rho}}\frac{d}{dz}\vec{F}_m \\ \frac{d\bar{T}}{dt} &= -\frac{1}{\bar{\rho}}\frac{d}{dz}\overline{w'T'}. \end{aligned} \tag{1.14}$$

Equations (1.13) and (1.14) indicate that if the momentum or heat flux is constant with altitude, then the drag or the heating, respectively, is zero. Therefore, since the momentum and heat flux are constant for an internal GW under the linear theory, there can only be significant acceleration, heating, or cooling of the background flow if a GW is dissipating or breaking. An important consequence of this result is that fully ducted waves do not deposit momentum or heat flux to the background atmosphere. Since computational limits prevent the inclusion of the effects of individually resolved GW events on the mean circulation in global climate models, the parameterization of GW effects in such models must account for ducted waves. We must therefore seek to understand the processes by which waves become ducted in the MLT region.

2. Instrumentation and Methodology

2.1 Instruments

Ground-based remote sensing instruments are powerful tools for observing the characteristics of the atmosphere in the MLT region at high temporal and spatial resolution within a localized area. In the following subsections, the instruments used to obtain the data used in this thesis will be introduced and discussed.

2.1.1 Sodium Lidar

Sodium (Na) resonance-fluorescence lidars are active remote sensing instruments which can measure the vertical structure of key atmospheric properties in the 80–105 km MLT region, including temperature, vertical winds, and horizontal winds. The large effective backscattering cross-section of sodium and relative abundance of sodium atoms in the MLT due to the persistent global sodium layer near ~92 km make sodium a very useful tracer for resonance-fluorescence lidars deployed all over the planet.

The primary instrument used to acquire the data used in this thesis is a narrow-band sodium lidar operated by the University of Illinois at Urbana-Champaign (UIUC) at the Andes Lidar Observatory (ALO) on Cerro Pachón, Chile (30.0° S, 70.0° W). At ALO, a pulsed frequency-doubled neodymium-doped yttrium-aluminum garnet (Nd:YAG) seed laser beam is passed through a pulsed dye laser amplifier before it is transmitted into the night sky. The lidar is tuned to the sodium D_{2a} transition at 589.158 nm using a sodium vapor cell, and an acousto-optic modulator continually adjusts the frequency between the line center and two frequencies which are offset from the line center by $\pm$630 MHz. The beam of photons is partially backscattered by resonant fluorescence processes in the sodium layer, and the backscattered photons are collected by four telescopes with diameters of 75 cm. The telescopes are pointed in fixed directions, with each telescope pointing at the zenith, and 20° off zenith in the south (S), east (E), and west (W) directions. The configuration allows the measurement of atmospheric temperature and line-of-sight (LOS)

winds through a three-frequency technique which determines the shape of the absorption spectrum [She and Yu, 1994]. The principle behind the technique is an inverse parameter extraction based on the thermal Doppler broadening of the sodium D_{2a} line shape resulting from the atmospheric temperature and the Doppler shift of the line center resulting from the mean LOS winds. In general, the zonal and meridional wind measurements are decomposed from the off-zenith wind measurements using simple trigonometry, but on the night of January 18, 2015 (20150118), analyzed in this thesis, the lidar was operated in zenith-only mode. As a result, only temperature, vertical wind, and sodium density profiles were measured. The raw data were gridded into 6 minute temporal bins and 500 m spatial bins to reduce measurement inaccuracy while maintaining reasonably high temporal and spatial resolution. The temperature and vertical wind data were used in Section 3.1 to calculate spatial and temporal profiles of the background atmosphere and to extract GW perturbations for the ducted wave event discussed in Section 3.2.

2.1.2 All-Sky Airglow Imager

Airglow emissions in the upper atmosphere are the result of chemiluminescent processes occurring inside layers of constituents such as neutral atomic oxygen (OI) and hydroxyl (OH) radicals. There are two major airglow emissions which originate in the mesopause region. The brightest emission comes from the OH Meinel band radiation in the near-infrared (0.7–4.0 μm) centered at an altitude of ~87 km. The OI green line at 557.7 nm near ~96 km is also useful for GW observations, though the noise level is typically higher than for the OH emissions. Variations in the emission intensity of both lines have been used to infer GW properties in the MLT region [e.g., Ejiri et al., 2003].

At ALO, the airglow imager uses a fish-eye lens with a field-of-view (FOV) of ~160° to measure the emission from the whole sky. The emissions are focused down onto a cooled charge-coupled focal-plane array (CCD). Two filters are used to alternately capture the OH and OI emissions on nights during low moon periods year-round. The size of the CCD is 1024 x 1024, but each image was binned down to a

512 x 512 array in order to increase the signal-to-noise ratio (SNR). Differences between successive images were then taken to obtain difference images in which the GW activity can be clearly seen. The images were also compressed down to 341 x 341 in order to reduce the file size of movies made from the series of still images. The compression was acceptable because, in Section 3.1.4, the images were used only to observe the horizontal propagation of the wave qualitatively and to estimate approximate horizontal characteristics for the wave. In general, however, detailed analysis of airglow images relies on the well-defined physical connection between the image pixels and sky position. The connection is not necessarily maintained in a one-to-one fashion when the images are compressed.

Since the airglow images are distorted due to the fish-eye lens, the difference images were cropped into square 200 × 200 arrays centered on the zenith in order to observe only the portion of the image with relatively small distortion. The number of degrees in the FOV spanned by each pixel is constant, so distortion was accounted for in the measurements using simple trigonometry. The altitude of ALO is roughly 2.5 km, so the distances to the OH and OI layers are approximately 84.5 km and 93.5 km, respectively. The corresponding approximate horizontal scales spanned by the OH and OI images in Section 3.1.4 are 180 km × 180 km and 200 km × 200 km. A time series of the cropped OH difference images was used in Section 3.1.4 to obtain approximate horizontal information for the ducted wave event, including the horizontal wavelength and extrinsic (observed) phase speed.

2.2 Methods

Gravity wave perturbation profiles, in general, cannot always be resolved from unfiltered *T* and *w* profiles measured by the ALO lidar. The data set must be carefully analyzed and processed to obtain the perturbation profiles with minimal distortion and without loss of information. The mathematical methods used to obtain the GW perturbations in Section 3.1 are described in this section. Error considerations for the *T*, *w*, and derived parameters are also discussed.

2.2.1 Lomb-Scargle Periodogram

In an unfiltered temperature or vertical wind profile measured by the sodium lidar, the total signal profile in the frequency domain is composed of many different signals which, in general, have varying spectral amplitudes and phases. There is also always noise present at most or all frequencies since the measurements themselves have noise. For a given time series signal, the distribution of signal power over the frequency domain is known as the power spectrum, or power spectral density. In this definition, we refer to power as the generalized squared amplitude of an abstract signal (e.g., temperature or wind speed). In Chapter 1, we established that the perturbations associated with propagating GWs in the linear theory are sinusoidal. The power spectrum of a perfect sinusoid is a Dirac delta function at the frequency of the sinusoid. In the real atmosphere, however, observed GWs generally do not behave perfectly sinusoidally. A quasi-monochromatic GW is one which has a power spectrum dominated by a single, relatively isolated frequency peak with a sufficiently small FWHM. Consequently, when a quasi-monochromatic GW with a sufficiently large perturbation amplitude is present in an observation window, the power spectrum of the signal will exhibit a peak centered on the frequency of the GW.

Lomb-Scargle periodograms are a useful tool for power spectral density estimation. Consider a set of *N* observations, x_k, which are taken at the time series t_k, where $k = 1, 2, \dots, N$. The Lomb-Scargle periodogram is defined by [Lomb, 1976]

$$P_{LS}(f) = \frac{1}{2\sigma^2}\left\{\frac{\left[\sum_{k=1}^{N}(x_k - \bar{x})\cos\big(\omega(t_k - \tau)\big)\right]^2}{\sum_{k=1}^{N}\cos^2\big(\omega(t_k - \tau)\big)} + \frac{\left[\sum_{k=1}^{N}(x_k - \bar{x})\sin\big(\omega(t_k - \tau)\big)\right]^2}{\sum_{k=1}^{N}\sin^2\big(\omega(t_k - \tau)\big)}\right\}, \tag{2.1}$$

where ω is the angular frequency, $\bar{x}$ and σ^2 are respectively the mean and variance of the set of observations, and τ is a time offset chosen such that the resulting power spectrum is time-invariant:

$$\tau = \frac{1}{2\omega}\tan^{-1}\left(\frac{\sum_{k=1}^{N}\sin(2\omega t_k)}{\sum_{k=1}^{N}\cos(2\omega t_k)}\right). \tag{2.2}$$

Lomb-Scargle periodograms are useful because they can be used to test an evenly or unevenly sampled time series for the presence of sinusoidal signals. A Lomb-Scargle periodogram was used in Section 3.1.3 to identify the power spectral density signature of a strong quasi-monochromatic GW in both temperature and vertical wind lidar observations from ALO early in the night of 20150118.

2.2.2 Zero-Phase Bandpass Filter

Digital bandpass filters can be used to extract spectral information in a given frequency window from a time series signal. Once a GW has been identified in a given lidar or airglow data set through a frequency-domain analysis of lidar or airglow data, the perturbations must be extracted from the data using a bandpass filter. The choices of filter and method of filtering are important since certain filters and filtering methods have a more desirable amplitude or phase response in the pass-band than others. Chebyshev Type-II bandpass filters can be designed to have steep roll-off at the pass-band edges and flat pass-bands. The trade-off is that there are ripples in the stop-band, but since a properly designed bandpass filter may have attenuation of 10^{-3} or more in the stop-band, this is typically not an issue. The frequency-dependent gain of a Chebyshev Type-II high-pass or low-pass filter may be written as [Parks and Burrus, 1987]

$$G_n(\omega, \omega_0) = \frac{1}{\sqrt{1 + \frac{1}{\varepsilon^2 T_n^2\left(\frac{\omega}{\omega_0}\right)}}}, \tag{2.3}$$

where ε is the ripple factor, ω_0 is the cutoff frequency, and T_n is an nth order Chebyshev polynomial. A Chebyshev Type-II bandpass filter can be made by combining a high-pass and low-pass filter designed using Equation (2.3).

A temporal comparison of an unfiltered time series with a filtered time series may be misleading if the phase response of the filter, which may cause features to shift temporally in the filtered data, is not accounted for. For this reason, a filter with zero phase response is desirable since the temporal position of features in the data will remain unchanged after the filter is applied. A zero-phase filter can be

implemented practically by filtering the signal, reversing the filtered signal, passing the reversed filtered signal back through the filter, and then reversing that signal. To understand why this algorithm results in a zero-phase filter, consider a real-valued digital filter with an impulse response $h[t_k]$ and a set of observations $x[t_k]$, where t_k is the same time series described in Section 2.2.1. The Fourier transforms of $h[t_k]$ and $x[t_k]$ are respectively given by $H(e^{i\omega})$ and $X(e^{i\omega})$. The result of the first filter pass is $X(e^{i\omega})H(e^{i\omega})$. In the frequency domain, time reversal is equivalent to replacing ω with $-\omega$, and the result becomes $X(e^{-i\omega})H(e^{-i\omega})$. The next filter pass is another multiplication by $H(e^{i\omega})$, so the result becomes $X(e^{-i\omega})H(e^{-i\omega})H(e^{i\omega})$. Finally, the second time reversal gives the output

$$Y(e^{i\omega}) = X(e^{i\omega})H(e^{i\omega})H(e^{-i\omega}) = X(e^{i\omega})\left|H(e^{i\omega})\right|^2 \tag{2.4}$$

since $H(e^{-i\omega})$ is the complex conjugate of $H(e^{i\omega})$ for real-valued filter coefficients. Equation (2.4) indicates that the algorithm is equivalent to a filter with a frequency response of $\left|H(e^{i\omega})\right|^2$. Thus, the new transfer function is purely real-valued (zero-phase) with an amplitude equal to the squared magnitude of the original filter. The effective filter order is also twice the original filter order.

A zero-phase Chebyshev Type-II bandpass filter was applied in the time domain to extract the GW perturbations from ALO temperature and vertical wind lidar measurements. The base filter was a digital 7th order Chebyshev Type-II bandpass filter and the bandstops were placed at 27 min and 54 min with a minimum stop-band attenuation of 10^{-3}. The corresponding effective transfer function for the zero-phase filter, which has 80% cutoff frequencies at 31 min and 46 min, a minimum stop-band attenuation of 10^{-6}, and a flat passband, is shown in Figure 2.1.

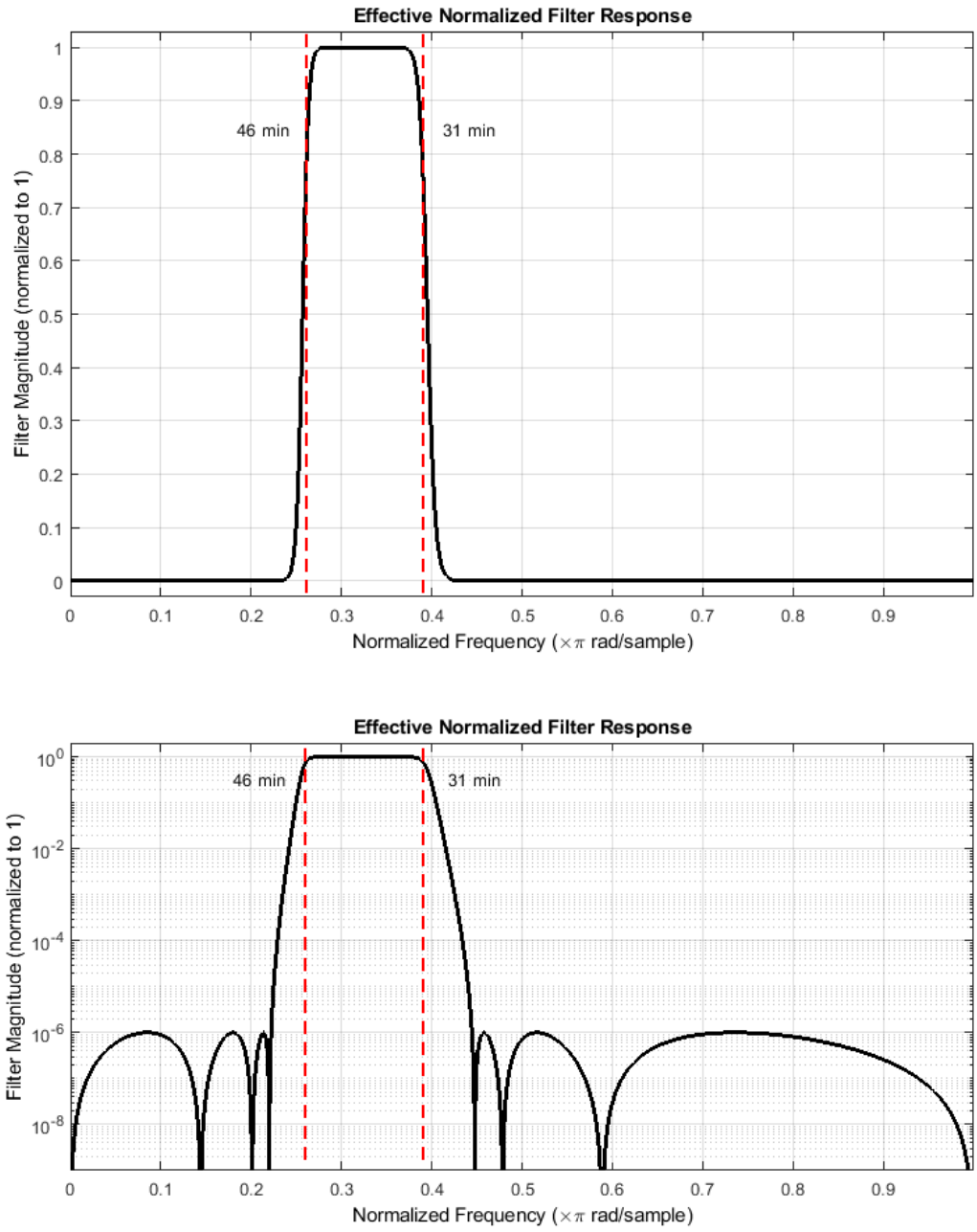

Figure 2.1 Effective normalized linear-scale (top) and logarithmic-scale (bottom) zero-phase bandpass filter response vs. frequency normalized to the Nyquist rate. The Nyquist rate for the ALO lidar data, which was sampled at 6 min intervals, is 0.0014 Hz. The vertical dashed red lines indicate the 80% cutoff frequencies of 31 min and 46 min.

2.2.3 Error and Error Propagation

There are various sources of error associated with any measurement. These errors must be considered when using data to derive parameters using a forward or inverse model. The errors associated with lidar temperature and wind measurements are dominated by shot noise resulting from the Poisson-distributed arrival of photons at the detector. If *N* photons arrive at the detector in one measurement interval, the corresponding standard Poisson measurement error is $\sqrt{N}$. The temperature and vertical wind uncertainties for the lidar measurements were derived based on the standard Poisson error and other sources of uncertainty such as laser tuning errors and laser linewidth fluctuations [Chu et al., 2002]. The uncertainties for the temperature and vertical wind data analyzed Chapter 3 are plotted in Figures 3.4 and 3.5. Quantities which are derived from measured quantities, such as the squared buoyancy frequency N^2 defined in Equation (1.7), will also have uncertainties associated with them which can be derived through an error propagation analysis. For an evenly sampled altitude grid, the uncertainty for N^2 is given by [Bossert et al., 2014]

$$\Delta N^2 = N^2 \sqrt{\left(\frac{1}{\frac{dT}{dz} + \frac{g}{c_p}}\right)^2 \left(\frac{\sqrt{2}\Delta T}{dz}\right)^2 + \left(\frac{\Delta T}{\bar{T}}\right)^2}, \tag{2.5}$$

where $\frac{dT}{dz}$ is the temperature gradient with altitude, dz is the altitude spacing, ΔT is the temperature uncertainty, and $\bar{T}$ is a suitable rolling-averaged temperature. In Section 3.1.2, N^2 was calculated based on the observed vertical temperature profile measured by the ALO lidar. The rolling altitude average used extended to one data point on each side of the temperature data point. The corresponding uncertainty ΔN^2 is plotted in Figure 3.8.

3. Analysis of a Ducted Wave Event

3.1 Data

In this section, lidar and airglow observations made at Andes Lidar Observatory (ALO) on Cerro Pachón, Chile (30.0° S, 70.0° W), on the night of January 18, 2015, are presented. The data are also processed using the methods described in Chapter 2 to extract GW parameters for the ducted wave event.

3.1.1 Lidar Measurements

On the night of January 18, 2015 (20150118), the ALO lidar was operated in zenith mode between 0.8 Universal Time (UT) and approximately 9.0 UT. Vertical profiles of sodium density, atmospheric temperature, and mean vertical wind were acquired over an altitude range of approximately 85–110 km. The spatial and temporal sampling rates for the data are respectively 500 m and 6 minutes. Since the number of backscattered photons from a particular altitude window is proportional to the number of sodium atoms at that altitude, a vertical profile of the sodium density is shown in Figure 3.1 to provide an indication of the altitude range over which the lidar signal is particularly strong. The temperature and vertical wind profiles are respectively shown in Figures 3.2 and 3.3, and their corresponding uncertainties are shown in Figures 3.4 and 3.5. In each figure, the starting and ending times of the displayed observation window are 0.8 UT and 3.5 UT, which respectively correspond to the beginning of the observations for the night and the approximate end of the ducted GW event discussed in Section 3.2. The perturbations associated with the ducted GW are clearly visible in the unfiltered vertical wind data in Figure 3.3, though the perturbations are not visually resolved in the unfiltered temperature data in Figure 3.2.

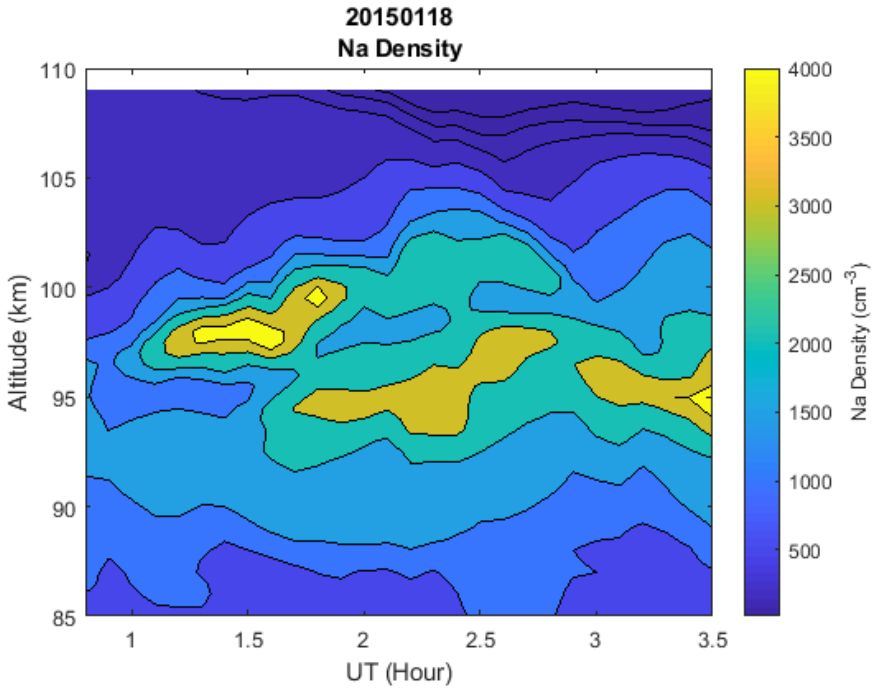

Figure 3.1 Lidar-measured sodium density contours for the observation window of 85–109 km and UT 0.8–3.5 on the night of 20150118. The peak of the layer near 98 km is high compared to the typical peak of ~92 km and the layer is relatively diffuse. The result is a good signal over an altitude range of approximately 85–105 km.

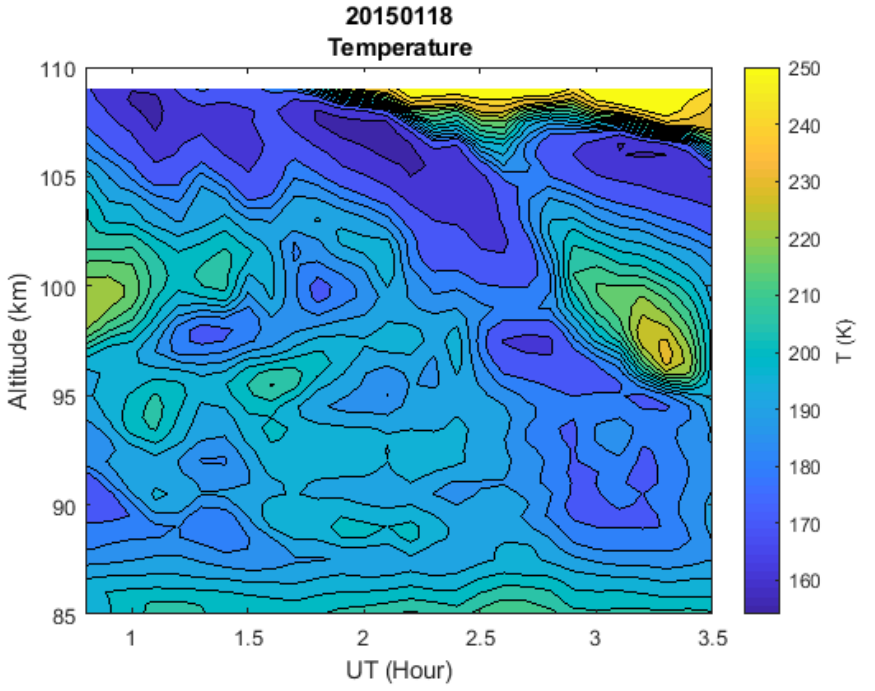

Figure 3.2 Same as Figure 3.1, but with temperature contours. The GW perturbations are too small to be resolved visually (without the aid of a filter) in the temperature profile. Note the large temperature change around 95–100 km towards the end of the observation window shown.

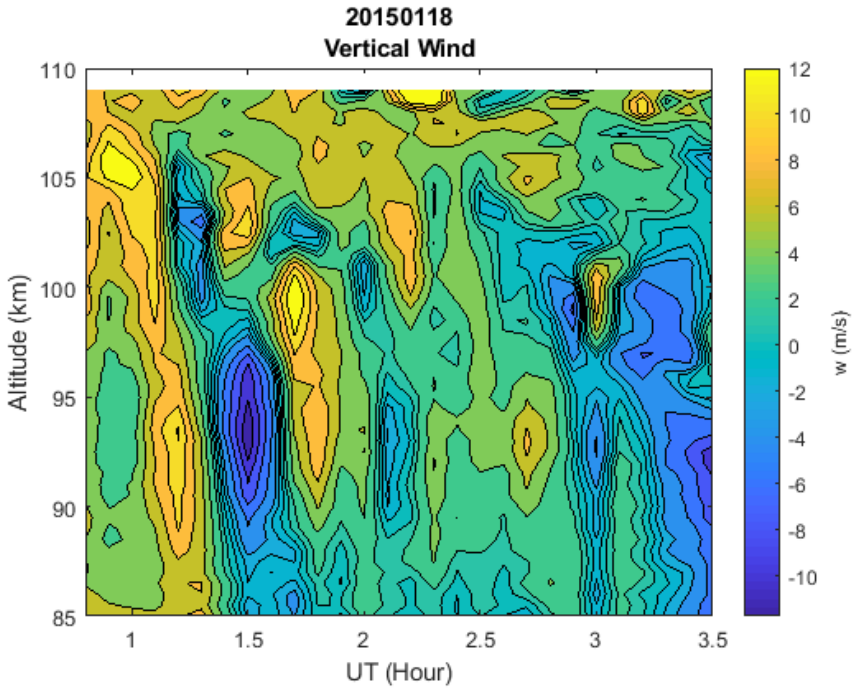

Figure 3.3 Same as Figure 3.1, but with vertical wind contours. The GW perturbations are large enough to be visually resolved in the unfiltered vertical wind data at ~1–2 UT near 90–95 km.

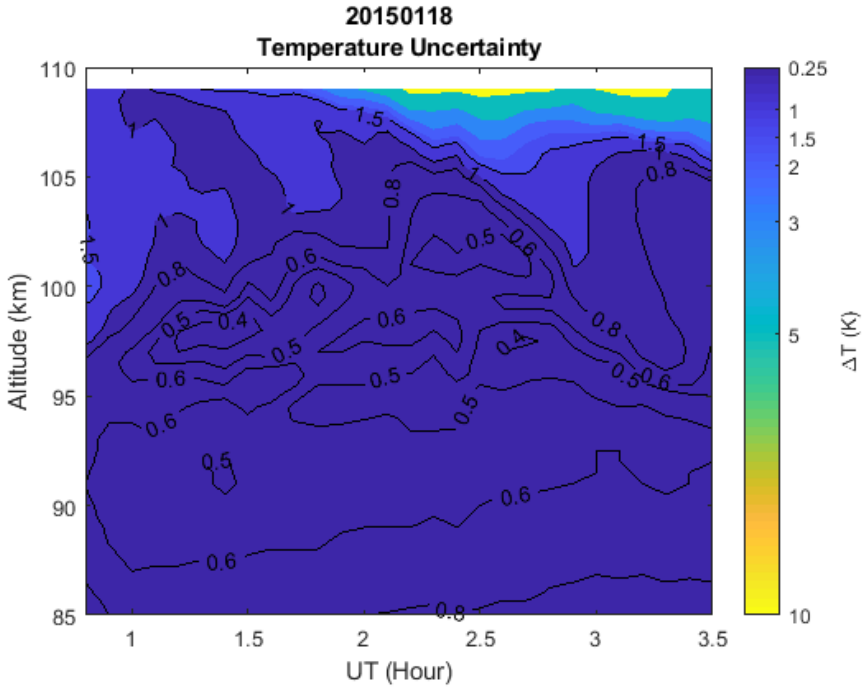

Figure 3.4 Measured temperature uncertainties in the observation window considered in Figure 3.1–3.3. The temperature uncertainty remains below 1 K for altitudes of roughly 85–103 km.

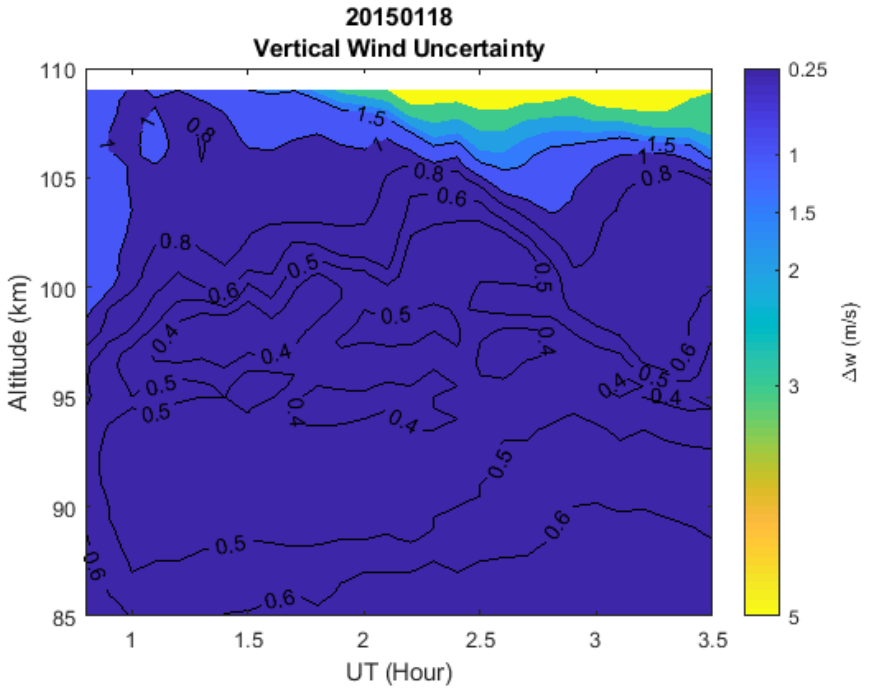

Figure 3.5 Same as Figure 3.4, but with measured vertical wind uncertainties. The vertical wind uncertainties remain below 1 m/s for most of the observation window below 105 km.

3.1.2 Background Atmosphere Characteristics

Case studies of individual GW events must take the background atmosphere, through which the wave propagates, into consideration. Two parameters which can be used to characterize the background atmosphere are the mean temperature profile in altitude, shown in Figure 3.6, and the N^2 profile over the observation window. The N^2 profile was calculated using Equation (1.7) and is shown in Figure 3.7. A profile of its corresponding uncertainty $|\Delta N^2|$ was calculated using Equation (2.5) and is shown in Figure 3.8. In the first portion of the observation window (0.8–2.0 UT), there are two distinct temperature inversions below the omnipresent lower thermospheric inversion (LTD). In the latter portion of the observation window (2.1–3.5 UT), there is only a single additional inversion. All the inversions correlate well with regions of high static stability ($N^2 \gg 0$) in Figure 3.7.

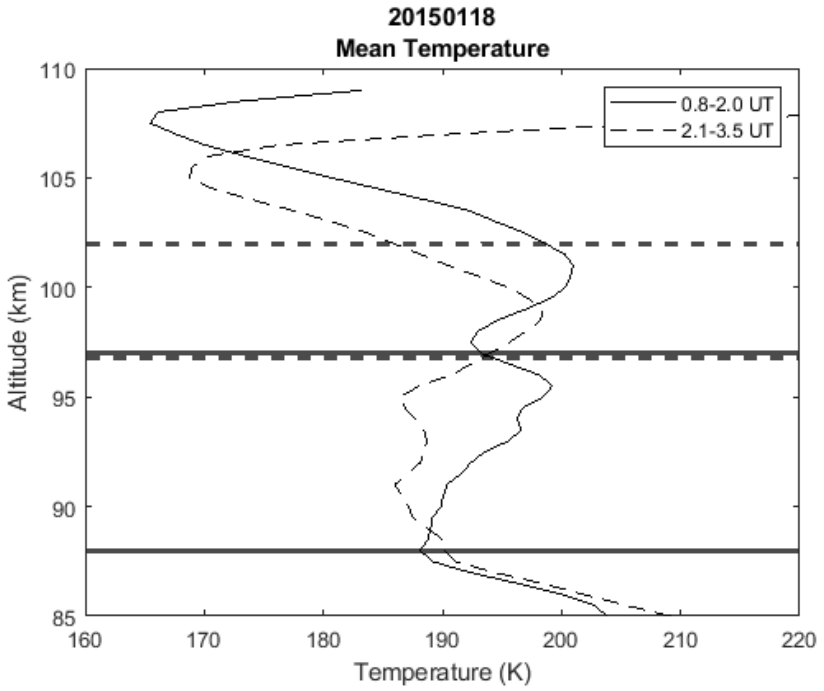

Figure 3.6 Time-averaged temperature profiles in the observation window. The mean temperatures were calculated separately for two time ranges in the observation window: 0.8–2.0 UT (solid curve), and 2.1–3.5 UT (dashed curve). The solid and dashed horizontal lines, which correspond to the same time ranges as the solid and dashed curves respectively, represent the approximate vertical extent of the GW *w'* perturbations shown in Figure 3.12.

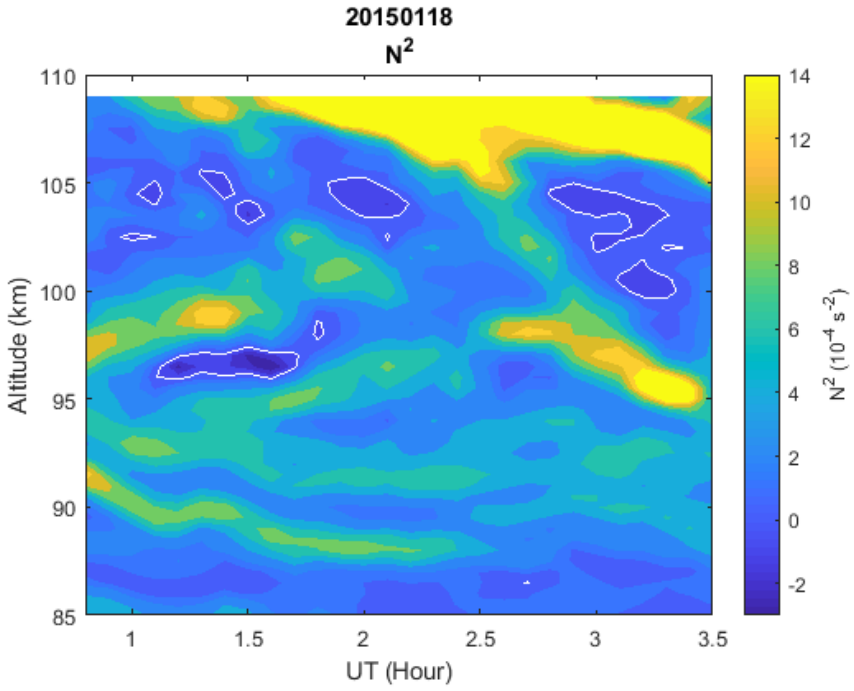

Figure 3.7 N^2 contours for the observation window calculated using Equation (1.7). Regions where N^2 is less than zero (inside white contours) are indicative of static instability. The observation window is relatively unstable, although there are regions of high stability at altitudes which correlate well with the inversions in Figure 3.6.

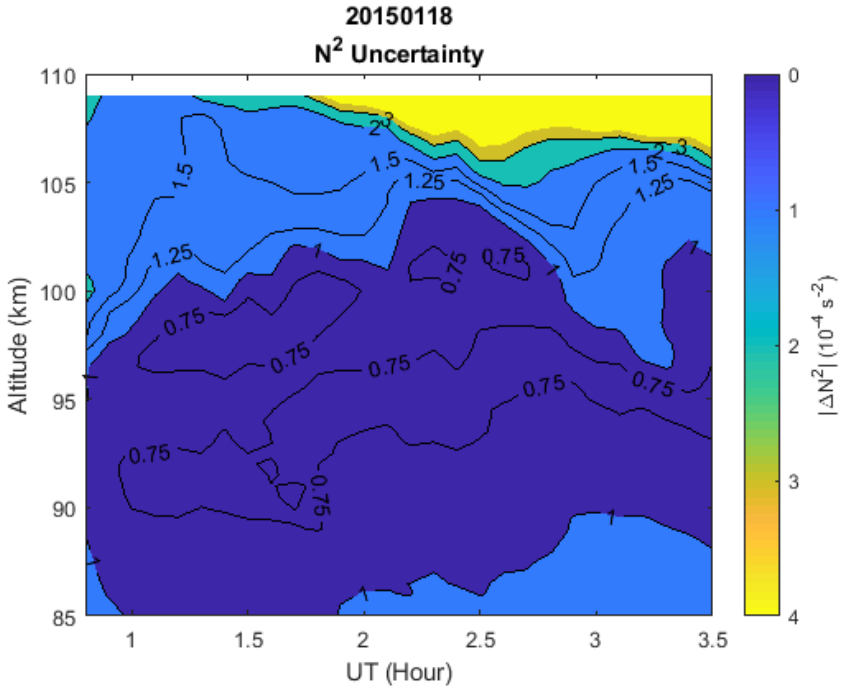

Figure 3.8 Contour plot of the corresponding uncertainty in the N^2 profile, calculated using Equation (2.5). The uncertainty in N^2 below approximately 105 km is acceptably low.

3.1.3 Gravity Wave Perturbations

In order to design the bandpass filter used to extract the GW perturbations from the temperature and vertical wind profiles shown in Figures 3.2 and 3.3, a Lomb-Scargle analysis of the power spectrum of each profile was carried out. A Lomb-Scargle periodogram defined by Equations (2.1) and (2.2) was applied to the time series data in the whole observation window (0.8–3.5 UT) at each altitude. The results of the Lomb-Scargle analysis are shown in Figures 3.9 and 3.10. The signature of a quasi-monochromatic GW was observed in the temperature spectrum and especially the vertical wind spectrum with a period of around 40 minutes. The zero-phase bandpass filter used to extract the GW perturbations, which is shown in Figure 2.1, was designed to extract most of the power associated with the GW perturbations while ensuring that longer-period noise sources were sufficiently attenuated by the filter. The loss in signal power resulting from the filter mismatch at periods near 50 minutes is acceptable since the perturbation magnitudes associated with the ducted GW event are large.

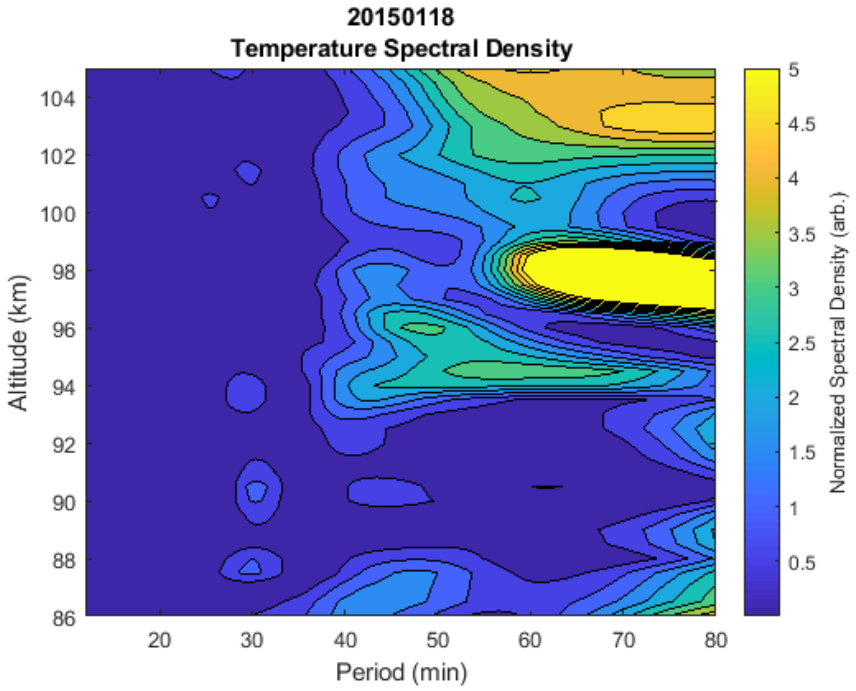

Figure 3.9 Contour plot of the Lomb-Scargle temperature power spectral density calculations for the observation window. The units are arbitrary but normalized to twice the variance of the signal. Only the subset of the data containing the GW peak is shown. The large amplitude in the 60–80 minute band near 98 km is an artefact resulting from the large temperature change towards the end of the observation window in Figure 3.2.

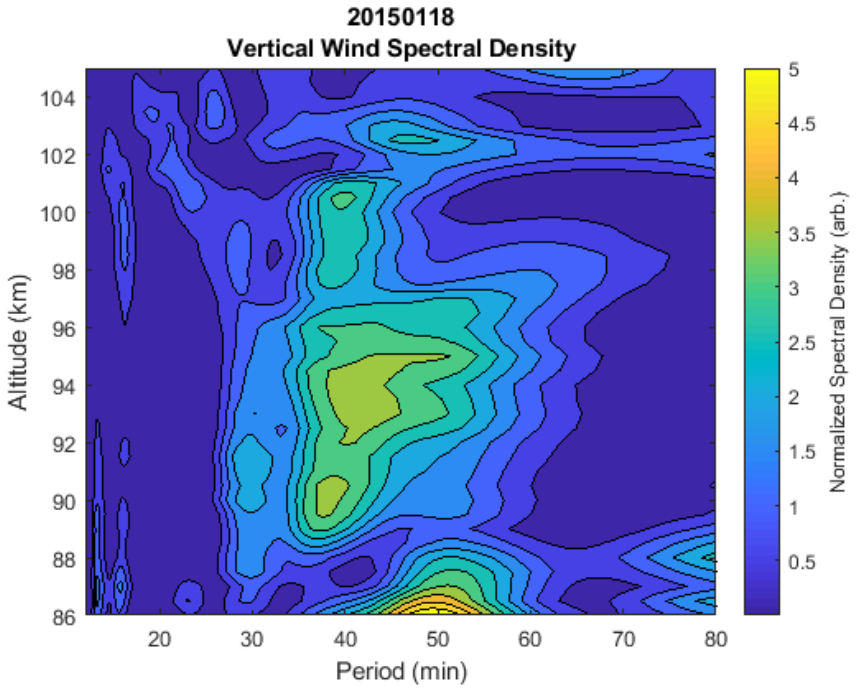

Figure 3.10 Same as Figure 3.9, but for the vertical wind power spectrum. The 40-minute peak is more prominent in the vertical wind spectrum and is consistent with the presence of a quasi-monochromatic GW signature.

The GW perturbations extracted from the temperature and vertical wind data are shown in Figures 3.11 and 3.12. The perturbation amplitudes are very large; the maximum temperature perturbation (*T'*) is approximately 8 K and the maximum vertical wind perturbation (*w'*) is nearly 7 m/s. The perturbations exhibit coherent phase characteristics, and all the observations, which are discussed in detail in Section 3.2, suggest that a ducted wave event with unique characteristics has been identified. Combined plots of the temperature and vertical wind perturbations for each altitude are provided for reference in Appendix A since the phase and amplitude relationships between the *T'* and *w'* perturbations are more easily observed at each individual altitude in the observation window.

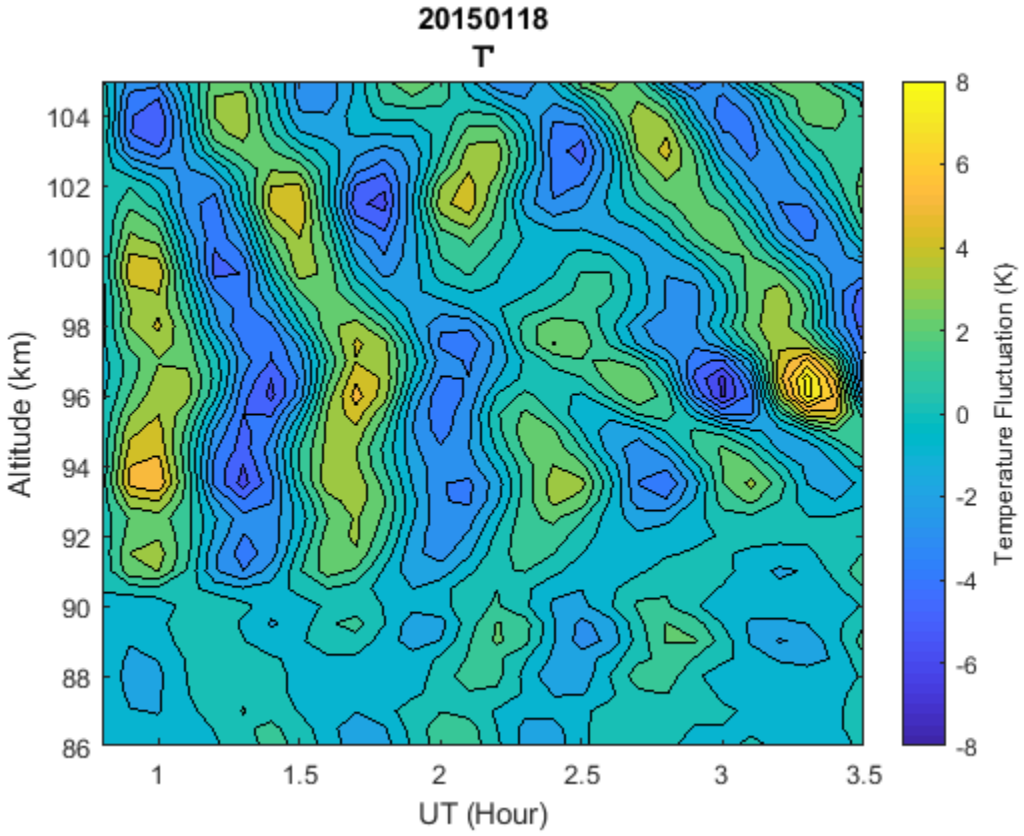

Figure 3.11 Contour plot of the *T'* perturbations associated with the GW ducting event. The magnitudes of the *T'* perturbations are large above approximately 90 km from 0.8 to 2.0 UT, and the approximately vertical phase structure at 91–97 km in the same time range suggests that the wave is at least partially ducted. The large-amplitude feature near 96–98 km towards the end of the observation window is most likely an artefact of the large temperature swing in the same region shown in Figure 3.2.

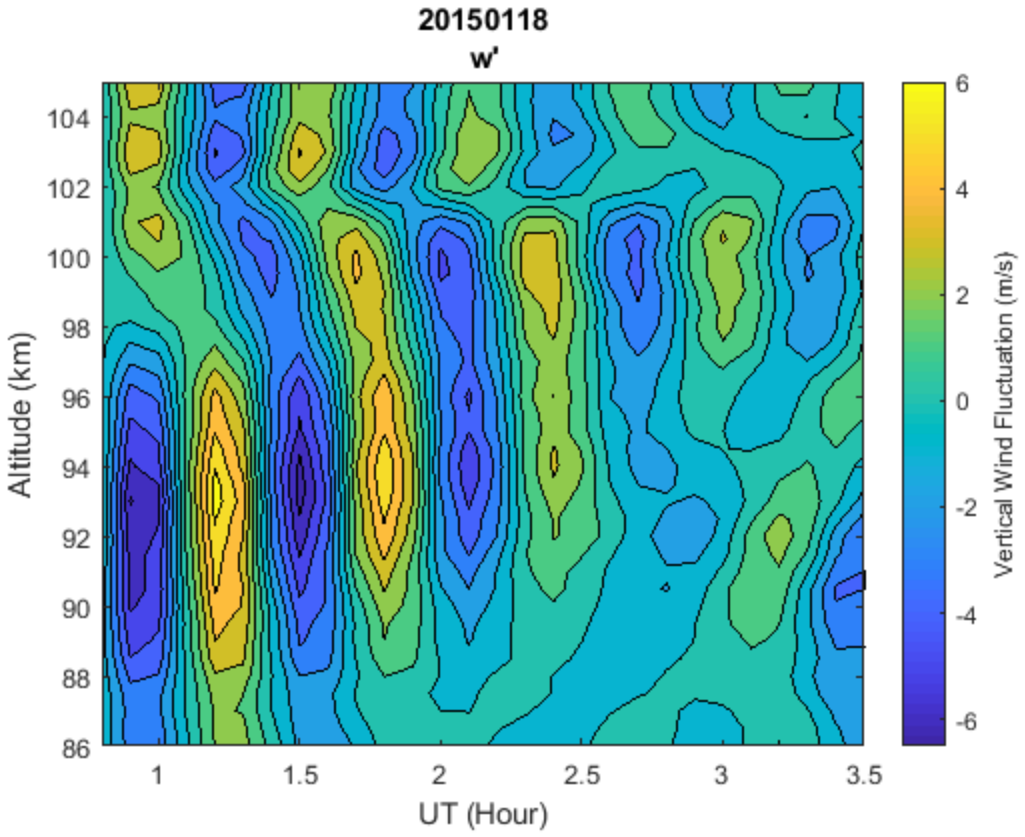

Figure 3.12 Same as Figure 3.11, but for the *w'* perturbations. The general structure of the *w'* perturbations is similar to the structure of the *T'* perturbations in Figure 3.11. The phase structure is nearly vertical in the same region as the *T'* perturbations.

3.1.4 Horizontal Wave Characteristics

Horizontal information about the GW ducting event was obtained through simultaneous airglow observations from the all-sky camera at ALO. The OH and OI difference images used to estimate the horizontal wavelength and extrinsic phase speed are shown in series in Figures 3.13 and 3.14. In both sets of images, the wave front was observed propagating directly southwest (SW). The horizontal wavelength was estimated from the OH image series to be ~40 km by measuring the pixel location of the back of successive wave fronts and calculating the physical distance on the image plane. The image distortion, which causes pixels near the center of the image to represent a smaller length than pixels near the edge, was accounted for by measuring the pixels relative to the zenith pixel of the image and using simple

trigonometry. The altitude of the OH layer in the images was estimated to be 88.5 km above the altitude of ALO since the *T′* perturbations in Figure 3.11 only have significant magnitude above 91 km. The extrinsic phase speed of the wave was estimated similarly using the time difference between successive passages of the wave front past the zenith pixel and the result was ~90 m/s in the SW direction.

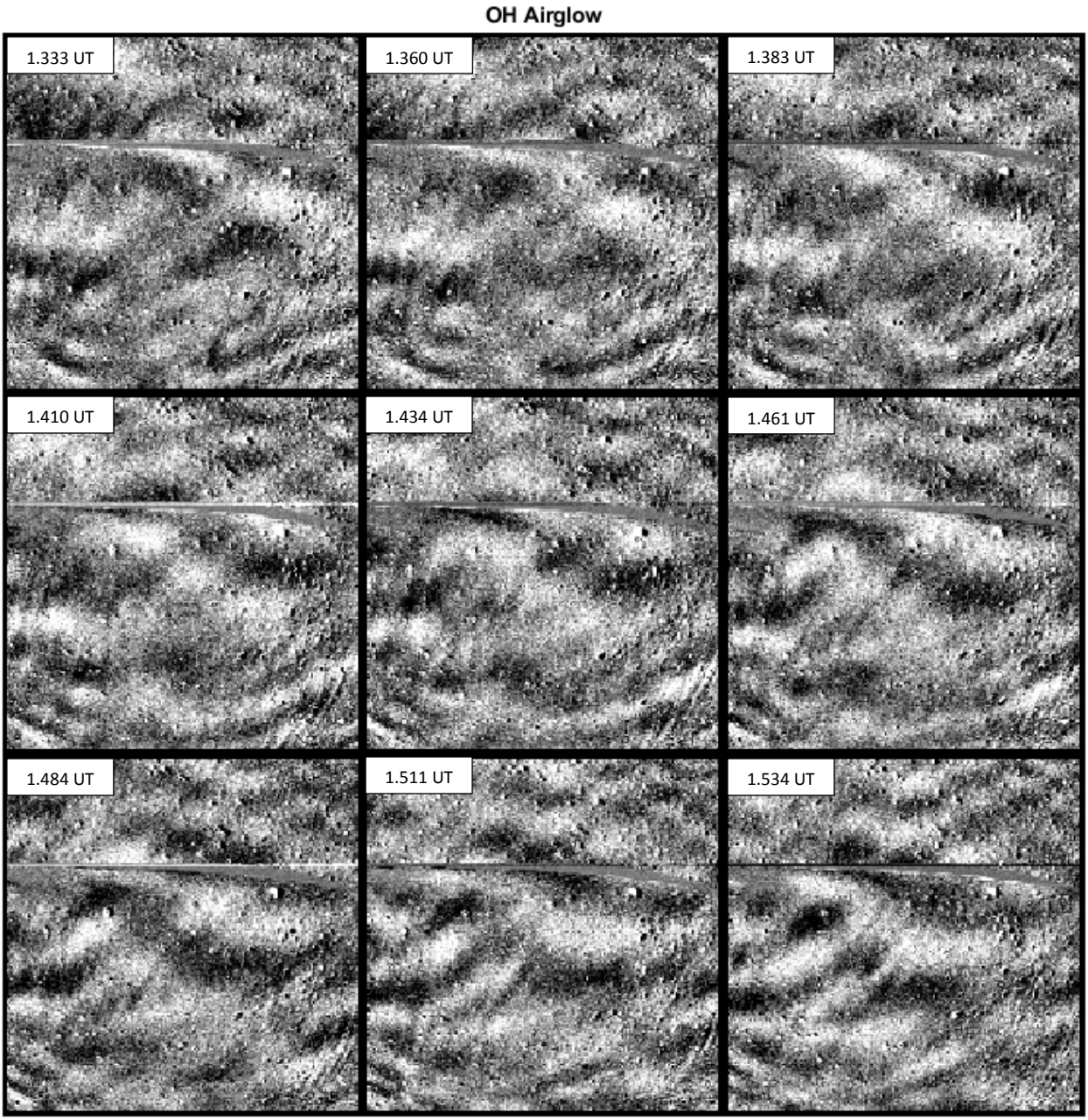

Figure 3.13 Series of OH airglow images taken concurrently with the lidar observations. Images were taken approximately 90 seconds apart and the zenith is located at the center pixel. N and E directions are at the top and right side of the images respectively. The total physical image size is approximately 180 km × 180 km.

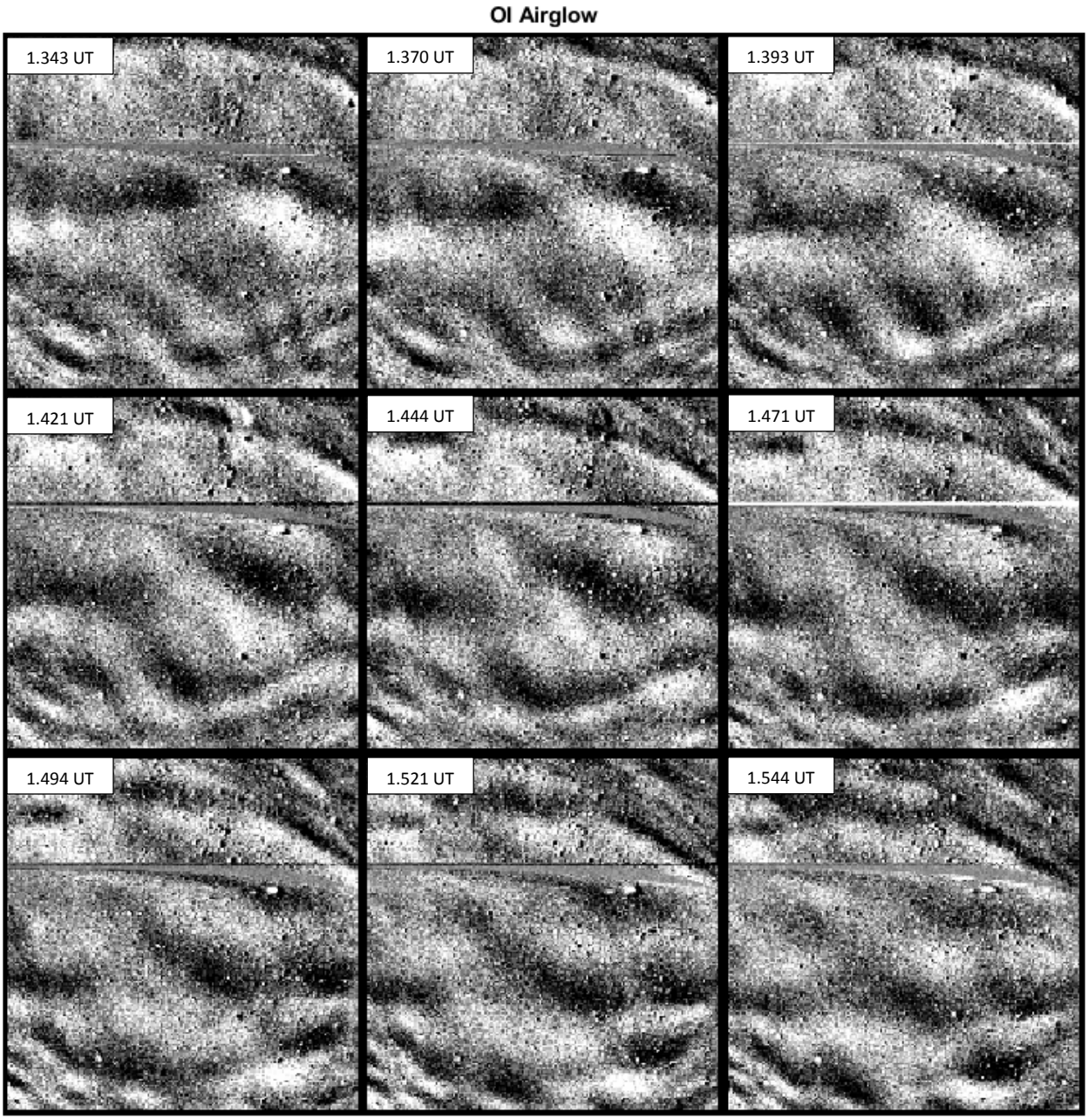

Figure 3.14 Same as Figure 3.13, but with OI airglow images. The wave front can also be seen propagating in the SW direction, though the wave fronts are less defined because the OI signal was lower than the OH signal. Since the altitude of the OI layer is approximately 96 km, the total physical image size is approximately 200 km × 200 km.

Since the lidar was operated in zenith mode during the observation window, horizontal wind measurements are unfortunately unavailable. In order to estimate the intrinsic phase speed of the GW, the latest Horizontal Wind Model (HWM14) [Drob et al., 2015] was used to approximate the mean

background zonal and meridional winds during the observation window. The results of the model are shown in Figures 3.15 and 3.16. However, the HWM14 model is a climatological model, so the predictions should in no way be taken as absolute since the real winds could differ significantly from the model for events occurring on the scale of a few hours.

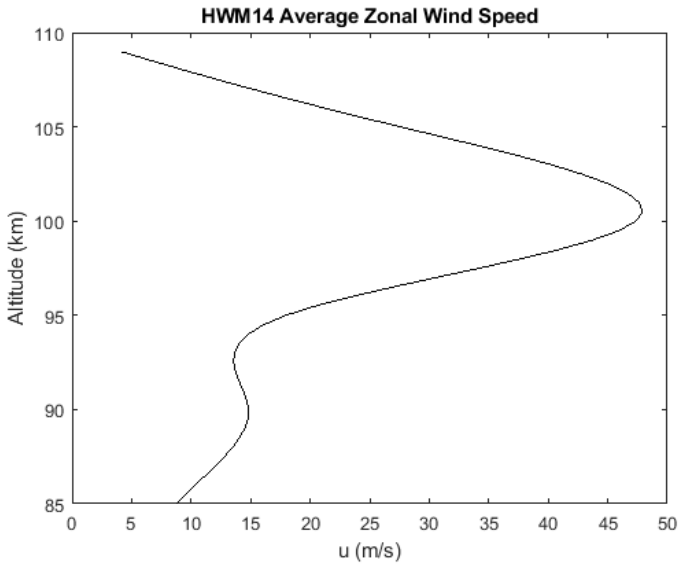

Figure 3.15 HWM14 zonal wind predictions for the night of 20150118. The HWM14 winds were time-averaged over the whole observation window (0.8–3.5 UT). The zonal wind speed is defined to be positive when the winds are blowing from the west.

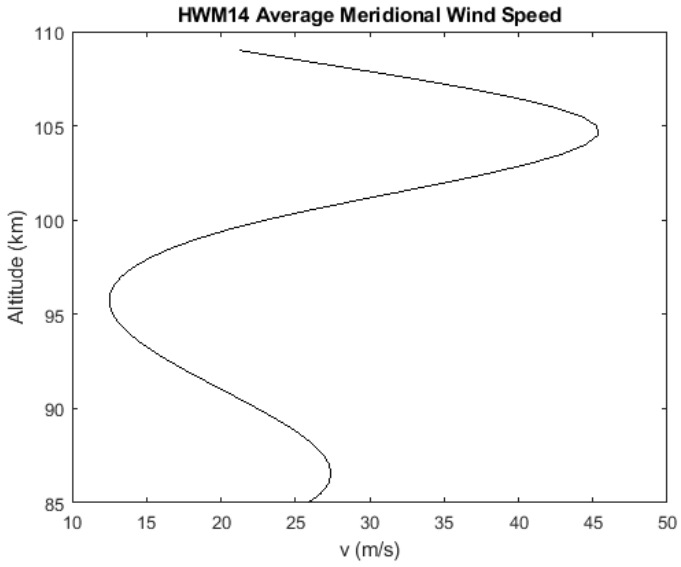

Figure 3.16 Same as Figure 3.15, but for the meridional wind predictions. The meridional wind speed is defined to be positive when the winds are blowing from the south.

3.2 Discussion

In this section, the GW perturbations and horizontal characteristics obtained in Section 3.1 are analyzed in the context of the background atmosphere in the observation window. The results strongly suggest that a ducted GW event occurred on the night of 20150118 at approximately 0.8–2.0 UT. The strongest evidence of GW ducting in this case is that both the *T'* and *w'* perturbations (Figures 3.11 and 3.12) in that time range were strong and aligned with each other nearly vertically within the 90–96 km altitude range. Since a significant temperature inversion was present at the same altitude range in the mean temperature profile (Figure 3.6) at 0.8–2.0 UT, we may conclude that thermal ducting processes were a major contributor to the ducting of the observed wave. The strong unstable layer near 96 km at 0.8–2.0 UT (see Figure 3.7) was the top edge of the thermal duct. There was also a layer of relatively low stability at the bottom of the observation window near 86 km which was most likely the bottom edge of the thermal duct. However, the ducted perturbation amplitudes began to decay after approximately 2.0 UT. The inversion and stability structures in Figures 3.6 and 3.7 changed significantly after that time, which implies that the resonant ducting conditions were no longer met, and the wave could not freely propagate. The perturbation amplitudes decayed greatly from their original magnitude by 3.5 UT. The results indicate that the ducting structure changed significantly on a timescale of one hour.

Comparison of the relative phase of the *T'* and *w'* perturbations in Figures 3.11 and 3.12 (see Appendix A) for the ducted GW indicates a phase relationship between the perturbations which is largely consistent with the linear gravity wave theory. The ducted GW perturbations are approximately 90° out of phase with each other at 91–95 km and the perturbations begin to pull back into phase at 96 km. The phase relationships indicate that the wave is effectively freely propagating at 91–95 km and dissipation occurs in the highly unstable layer at 96 km. Furthermore, the perturbations in the 91–95 km altitude range after 2.0 UT are also in phase, which is consistent with the observed off-resonance dissipation of the wave. We may also consider the phase relationship between *T'* and *w'* above the highly unstable layer

at 96 km. The downward phase progression of both the *T'* and *w'* perturbations at 98–101 km indicates that some wave energy leaked out of the duct in the form of an upward-propagating wave. The phase difference between the perturbations is again approximately 90° in that altitude range, which is consistent with a freely propagating GW. However, above 102 km there was another highly unstable layer and the wave may have become ducted again until approximately 2.0 UT. The overall ducting structure for the observed event is highly complex and numerical modeling is necessary to provide further insight into the processes occurring in the event. It is also presently unclear whether or not the LTD played a role in the excitation of the resonant ducted GW. However, it appears that a secondary wave was generated by energy leakage from the primary duct, which suggests that a strong resonant GW ducting event can indirectly contribute a change to the total vertical momentum flux through secondary wave generation.

It is unclear whether the horizontal structure of the observed primary ducted GW is consistent with the linear GW theory. GWs, in the linear theory, have dispersion-imposed limits on their intrinsic phase speeds [Swenson et al., 2000]. The extrinsic phase speed of ∼90 m/s is fast enough that the intrinsic phase speed could be outside the dispersion-imposed limit depending on the real horizontal wind vector. The HWM14 wind predictions at 91 km are opposed to the propagation direction of the ducted GW with a total magnitude of ∼20 m/s. The resulting intrinsic phase speed of the ducted GW would be ∼110 m/s, which is outside the dispersion-imposed limit for a GW with horizontal wavelength of ∼40 km. Non-linear effects would have to be considered to explain such a large phase speed. However, if we instead assume no winds or winds opposite to the HWM14 winds, the intrinsic phase speed would respectively be at the edge of the dispersion-imposed limit or well within the limit. The squared vertical wavenumber m^2 associated with the GW as calculated by Equation (1.4) goes to zero in these cases, which would be consistent with a ducted GW in the linear theory. Thus, we cannot make any further conclusions about the consistency of the event with the linear GW theory without observations of the horizontal winds. However, the presence of both maxima and minima in the HWM14 wind profiles shown in Figures 3.15

and 3.16 indicates generally that there is a possibility that Doppler ducting also contributed to the observed GW ducting event. A comprehensive numerical modeling-based analysis of this event should therefore include the effects of Doppler ducting from multiple potential horizontal wind profiles in order to fully investigate the observed phenomenon. Future observations of similar events will benefit greatly from correlative lidar measurements of the vertical structure in the horizontal winds.

4. Conclusions

We have observed a highly resonant GW ducting event in the mesopause region above the Andes Lidar Observatory on the night of January 18, 2015, through correlative lidar and airglow observations. The analysis of the evolution of the *T'* and *w'* perturbations associated with the ducted wave provides insight into the resonant ducting of GWs in the MLT. The observed GW had a horizontal wavelength of ~40 km and an extrinsic phase speed of ~90 m/s. The data show that complex resonant thermal ducting structures associated with unstable layers in the atmosphere can dissipate on timescales on the order of one hour. The observed phase relationship between the *T'* and *w'* perturbations is largely consistent with the linear GW theory. Furthermore, evidence of the generation of a secondary upward-propagating GW was also found. The implication of this result is that the parameterization of GW effects in global climate models should ideally consider statistically both the ducted waves themselves as well secondary waves that may be generated. Further observations and modeling of similar GW ducting events are needed to better understand the processes involved. While thermal ducting was certainly a major contributor to the observed event, the lack of lidar-measured horizontal wind profiles for this event prevent drawing any conclusions about possible contributions by Doppler ducting. Off-zenith lidar measurements of the vertical structure of horizontal winds are therefore crucial to the further study of similar events. Additionally, numerical modeling-based analyses attempting to recreate the observed event should include horizontal wind profiles to understand the contribution of Doppler ducting to the event.

References

Andrews, D. G., Holton, J. R., & Leovy, C. B. (1987). *Middle Atmosphere Dynamics*. International Geophysics Series, vol. 40. Academic Press.

Bossert, K., Fritts, D. C., Pautet, P. D., Taylor, M. J., Williams, B. P., & Pendleton, W. R. (2014). Investigation of a mesospheric gravity wave ducting event using coordinated sodium lidar and mesospheric temperature mapper measurements at ALOMAR, Norway (69°N). *Journal of Geophysics Research: Atmospheres, 119*(16). 9765–9778. https://doi.org/10.1002/2014JD021460.

Bossert, K., Kruse, C. G., Heale, C. J., Fritts, D. C., Williams, B. P., Snively, J. B., et al. (2017). Secondary gravity wave generation over New Zealand during the DEEPWAVE campaign. *Journal of Geophysics Research: Atmospheres, 122*(15). 7834–7850. https://doi.org/10.1002/2016JD026079.

Cao, B. (2017). *Dynamical Processes of Gravity Waves Propagation and Dissipation, and Statistical Characteristics of Their Momentum Flux in the Mesosphere and Lower Thermosphere*. (Doctoral dissertation). Retrieved from Embry-Riddle Aeronautical University Scholarly Commons. (https://commons.erau.edu/edt/319/). Daytona Beach, FL: Embry-Riddle Aeronautical University.

Chimonas, G., & Hines, C.O. (1986). Doppler ducting of atmospheric gravity waves. *Journal of Geophysics Research: Atmospheres, 91*(D1). 1219–1230. https://doi.org/10.1029/JD091iD01p01219.

Chu, X., Pan, W., Papen, G. C., & Gardner, C. S. (2002). Fe Boltzmann temperature lidar: Design, error analysis, and initial results at the North and South Poles. *Applied Optics, 41*(21). 4400–4410. https://doi.org/10.1364/AO.41.004400.

Cohen, N. Y., Gerber, E. P., & Bühler, O. (2014). What drives the Brewer–Dobson circulation? *Journal of the Atmospheric Sciences, 71*(10). 3837–3855. https://doi.org/10.1175/JAS-D-14-0021.1.

Drob, D. P., Emmert, J. T., Meriwether, J. W., Makela, J. J., Doornbos, E., Conde, M., et al. (2015). An update to the Horizontal Wind Model (HWM): The quiet time thermosphere. *Earth and Space Science, 2*(7). 301–319. https://doi.org/10.1002/2014EA000089.

Ejiri, M. K., Shiokawa, K., Ogawa, T., Igarashi, K., Nakamura, T., & Tsuda, T. (2003). Statistical study of short-period gravity waves in OH and OI nightglow images at two separated sites. *Journal of Geophysical Research, 108*(D21). https://doi.org/10.1029/2002JD002795.

Ern, M., Ploeger, F., Preusse, P., Gille, J. C., Gray, L. J., Kalisch, S., et al. (2014). Interaction of gravity waves with the QBO: A satellite perspective. *Journal of Geophysical Research: Atmospheres, 119*(5). 2329–2355. https://doi.org/10.1002/2013JD020731.

Ern, M., Preusse, P., & Riese, M. (2015). Driving of the SAO by gravity waves as observed from satellite. *Annales Geophysicae, 33*(4). 483–504. https://doi.org/10.5194/angeo-33-483-2015.

Franke, P. M. & Robinson, W. A. (1999). Nonlinear behavior in the propagation of atmospheric gravity waves. *Journal of the Atmospheric Sciences, 56*(17). 3010–3027. https://doi.org/10.1175/1520-0469(1999)056<3010:NBITPO>2.0.CO;2.

Friedman, J. P. (1966). Propagation of internal gravity waves in a thermally stratified atmosphere. *Journal of Geophysical Research, 71*(4). 1033–1054. https://doi.org/10.1029/JZ071i004p01033.

Fritts, D. C. & Alexander, M. J. (2003). Gravity wave dynamics and effects in the middle atmosphere. *Reviews of Geophysics, 41*(1). https://doi.org/10.1029/2001RG000106.

Fritts, D. C. & Rastogi, P. K. (1985). Convective and dynamical instabilities due to gravity wave motions in the lower and middle atmosphere: Theory and observations. *Radio Science, 20*(6). 1247–1277. https://doi.org/10.1029/RS020i006p01247.

Fritts, D. C., Wang, L., & Werne, J. A. (2013). Gravity wave–fine structure interactions. Part I: Influences of fine structure form and orientation on flow evolution and instability. *Journal of the Atmospheric Sciences, 70*(12). 3710–3734. https://doi.org/10.1175/JAS-D-13-055.1.

Gardner, C. S. (2018). Role of wave-induced diffusion and energy flux in the vertical transport of atmospheric constituents in the mesopause region. *Journal of Geophysical Research: Atmospheres, 123*(12). 6581–6604. https://doi.org/10.1029/2018JD028359.

Gierasch, P., Goody, R., & Stone, P. (1970). The energy balance of planetary atmospheres. *Geophysical Fluid Dynamics, 1*(1–2). 1–18. https://doi.org/10.1080/03091927009365766.

Goldstein, S. (1931). On the stability of superposed streams of fluids of different densities. *Proceedings of the Royal Society of London A: Mathematical, Physical and Engineering Sciences, 132*(820). 524–548. https://doi.org/10.1098/rspa.1931.0116.

Guo, Y., Liu, A. Z., & Gardner, C. S. (2017). First Na lidar measurements of turbulence heat flux, thermal diffusivity, and energy dissipation rate in the mesopause region. *Geophysical Research Letters, 44*(11). 5782–5790. https://doi.org/10.1002/2017GL073807.

Hedin, A. E. (1991). Extension of the MSIS thermosphere model into the middle and lower atmosphere. *Journal of Geophysical Research: Space Physics, 96*(A2). 1159–1172. https://doi.org/10.1029/90JA02125.

Hedin, A. E., Fleming, E. L., Manson, A. H., Schmidlin, F. J., Avery, S. K., Clark, R. R., et al. (1996). Empirical wind model for the upper, middle, and lower atmosphere. *Journal of Atmospheric and Terrestrial Physics, 58*(13). 1421–1447. https://doi.org/10.1016/0021-9169(95)00122-0.

Hines, C. O. (1960). Internal atmospheric gravity waves at ionospheric heights. *Canadian Journal of Physics, 38*. 1441–1481. https://doi.org/10.1139/p60-150.

Hu, X., Liu, A. Z., Gardner, C. S., & Swenson, G. R. (2002). Characteristics of quasimonochromatic gravity waves observed with lidar in the mesopause region at Starfire Optical Range, NM. *Geophysical Research Letters, 29*(24). 2169. https://doi.org/10.1029/2002GL014975.

Khomich, V. Y., Semenov, A. I., & Shefov, N. N. (2008). *Airglow as an Indicator of Upper Atmospheric Structure and Dynamics*. Springer.

Liou, K.-N. (2002). *An Introduction to Atmospheric Radiation*. International Geophysics Series, vol. 84. Academic Press. 2nd ed.

Liu, H.-L., Hays, P. B., & Roble, R. G. (1999). A numerical study of gravity wave breaking and impacts on turbulence and mean state. *Journal of the Atmospheric Sciences, 56*(13). 2152-2177. https://doi.org/10.1175/1520-0469(1999)056<2152:ANSOGW>2.0.CO;2.

Liu, A. Z., Roble, R. G., Hecht, J. H., Larsen, M. F., & Gardner, C. S. (2004). Unstable layers in the mesopause region observed with Na lidar during the Turbulent Oxygen Mixing Experiment (TOMEX) campaign. *Journal of Geophysical Research: Atmospheres, 109*(D2). https://doi.org/10.1029/2002JD003056.

Liu, X., Xu, J., Yue, J., & Vadas, S. L. (2013). Numerical modeling study of the momentum deposition of small amplitude gravity waves in the thermosphere. *Annales Geophysicae, 31*(1). 1–14. https://doi.org/10.5194/angeo-31-1-2013.

Liu, H.-L., Bardeen, C. G., Foster, B. T., Lauritzen, P., Liu, J., Gang, L., et al. (2018). Development and validation of the Whole Atmosphere Community Climate Model With Thermosphere and Ionosphere Extension (WACCM-X 2.0). *Journal of Advances in Modeling Earth Systems, 10*(2). 381–402. https://doi.org/10.1002/2017MS001232.

Lomb, N. R. (1976). Least-squares frequency analysis of unequally spaced data. *Astrophysics and Space Science, 39*(2). 447–462. http://doi.org/10.1007/BF00648343.

Lu, X., Chen, C., Huang, W., Smith, J. A., Chu, X., Yuan, T., et al. (2015). A coordinated study of 1h mesoscale gravity waves propagating from Logan to Boulder with CRRL Na Doppler lidars and temperature mapper. *Journal of Geophysical Research: Atmospheres, 120*(19). 10,006–10,021. https://digitalcommons.usu.edu/envs_facpub/1479.

Nappo, C. (2012). *An Introduction to Atmospheric Gravity Waves.* International Geophysics Series, vol. 102. Academic Press.

Parks, T. W. & Burrus, C. S. (1987). *Digital Filter Design*. John Wiley and Sons, New York.

Plane, J. M. C., Feng, W., and Dawkins, E. C. M. (2015). The mesosphere and metals: Chemistry and changes. *Chemical Reviews, 115*(10). 4497–4541. https://doi.org/10.1021/cr500501m.

She, C.-Y., & Yu, J. (1994). Simultaneous three-frequency Na lidar measurements of radial wind and temperature in the mesopause region. *Geophysical Research Letters, 21*(17). 1771–1774. https://doi.org/10.1029/94GL01417.

Shimizu, A., & Tsuda, T. (1997). Characteristics of Kelvin waves and gravity waves observed with radiosondes over Indonesia. *Journal of Geophysical Research: Atmospheres, 102*(D22). 26159–26171. https://doi.org/10.1029/96JD03146.

Smith, S. M., Taylor, M. J., Swenson, G. R., She, C.-Y., Hocking, W., Baumgardner, J., & Mendillo, M. (2003). A multidiagnostic investigation of the mesospheric bore phenomenon. *Journal of Geophysical Research, 108*(A2). 1083. https://doi.org/10.1029/2002JA009500.

Smith, S. M., Friedman, J., Raizada, S., Tepley, C., Baumgardner, J., & Mendillo, M. (2005). Evidence of mesospheric bore formation from a gravity wave breaking event: simultaneous imaging and lidar measurements. *Journal of Atmospheric and Solar-Terrestrial Physics, 67*(4). 345–356. https://doi.org/10.1016/j.jastp.2004.11.008.

Swenson, G. R., Alexander, M. J., & Haque, R. (2000). Dispersion imposed limits on atmospheric gravity waves in the mesosphere: Observations from OH airglow. *Geophysical Research Letters, 27*(6). 875–878. https://doi.org/10.1029/1999GL010738.

Swenson, G. R., Liu, A. Z., Li, F., & Tang, J. (2003). High frequency atmospheric gravity wave damping in the mesosphere. *Advances in Space Research, 32*(5). 785–793. https://doi.org/10.1016/S0273–1177(03)00399-5.

Taylor, G. I. (1931). Effect of variation in density on the stability of superposed streams of fluid. *Proceedings of the Royal Society of London A: Mathematical, Physical and Engineering Sciences, 132*(820). 499–523. https://doi.org/10.1098/rspa.1931.0115.

Vadas, S. L. (2013). Compressible f-plane solutions to body forces, heatings, and coolings, and application to the primary and secondary gravity waves generated by a deep convective plume. *Journal of Geophysical Research: Space Physics, 118*(5). 2377–2397. https://doi.org/10.1002/jgra.50163.

Vadas, S. L., Fritts, D. C., & Alexander, M. J. (2003). Mechanism for the generation of secondary waves in wave breaking regions. *Journal of the Atmospheric Sciences, 60*(1). 194–214. https://doi.org/10.1175/1520-0469(2003)060<0194:MFTGOS>2.0.CO;2.

Vargas, F., Swenson, G. R., Liu, A. Z., & Pautet, P.-D. (2016). Evidence of the excitation of a ring-like gravity wave in the mesosphere over the Andes Lidar Observatory. *Journal of Geophysical Research: Atmospheres, 121*(15). 8896–8912. https://doi.org/10.1002/2016JD024799.

Walterscheid, R. L. (1981). Dynamical cooling induced by dissipating internal gravity waves. *Geophysical Research Letters, 8*(12). 1235–1238.

Walterscheid, R. L., & Hickey, M. P. (2009). Gravity wave ducting in the upper mesosphere and lower thermosphere duct system. *Journal of Geophysical Research: Atmospheres, 114*(D19). https://doi.org/10.1029/2008JD011269.

Xu, J., Liu, H.-L., Yuan, W., Smith, A. K., Roble, R. G., Mertens, C. J., et al. (2007). Mesopause structure from Thermosphere, Ionosphere, Mesosphere, Energetics, and Dynamics (TIMED)/Sounding of the Atmosphere Using Broadband Emission Radiometry (SABER) observations. *Journal of Geophysical Research, 112*(D9). https://doi.org/10.1029/2006JD007711.

Zhou, Q., & Morton, Y. T. (2007). Gravity wave propagation in a nonisothermal atmosphere with height varying background wind. *Geophysical Research Letters, 34*(23). https://doi.org/10.1029/2007GL031061.

Appendix A: Temperature and Vertical Wind Perturbations with Altitude

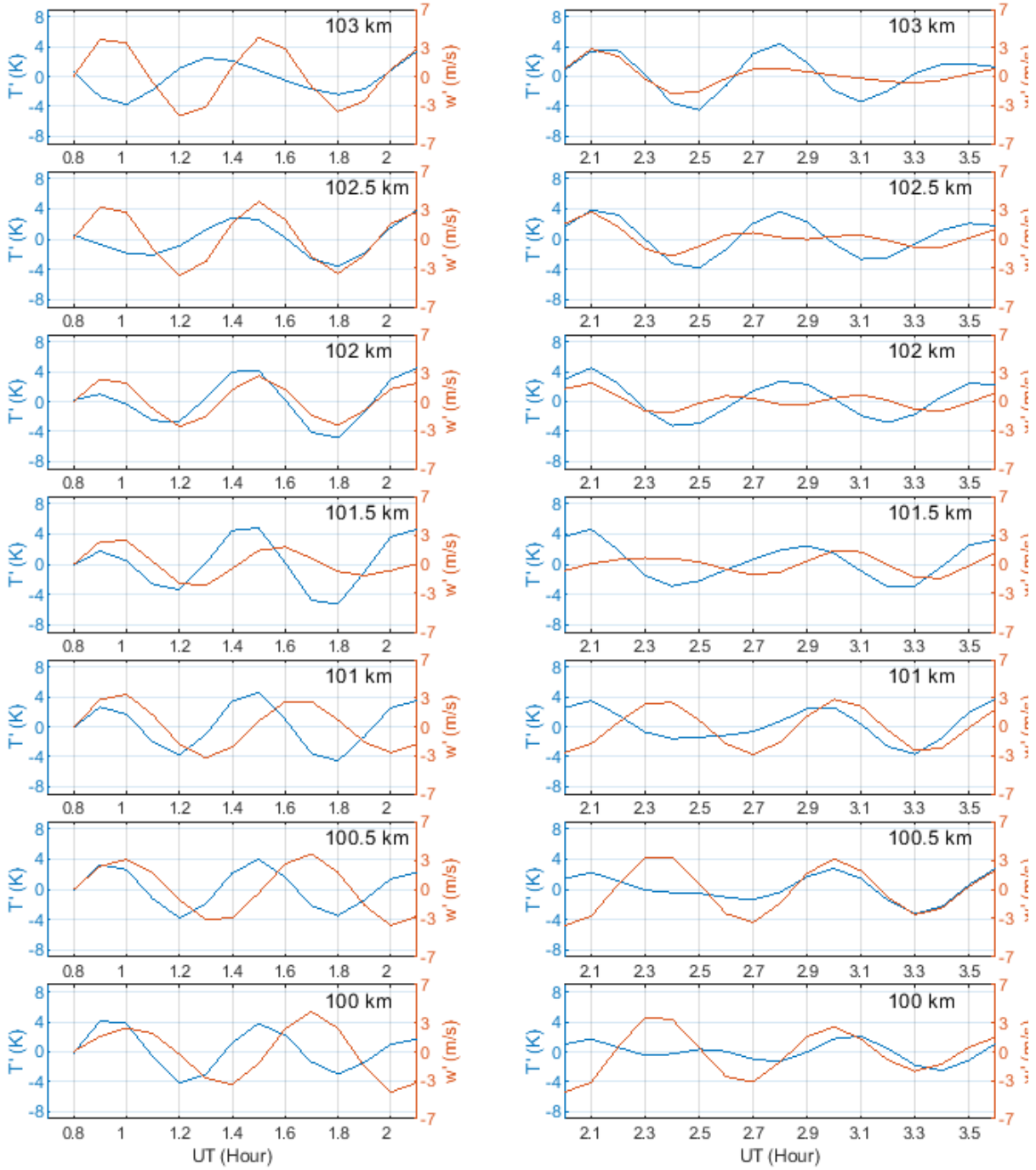

Figure A.1 Individual *T'* and *w'* profiles from Figures 3.11 and 3.12 for the altitude range 100–103 km.

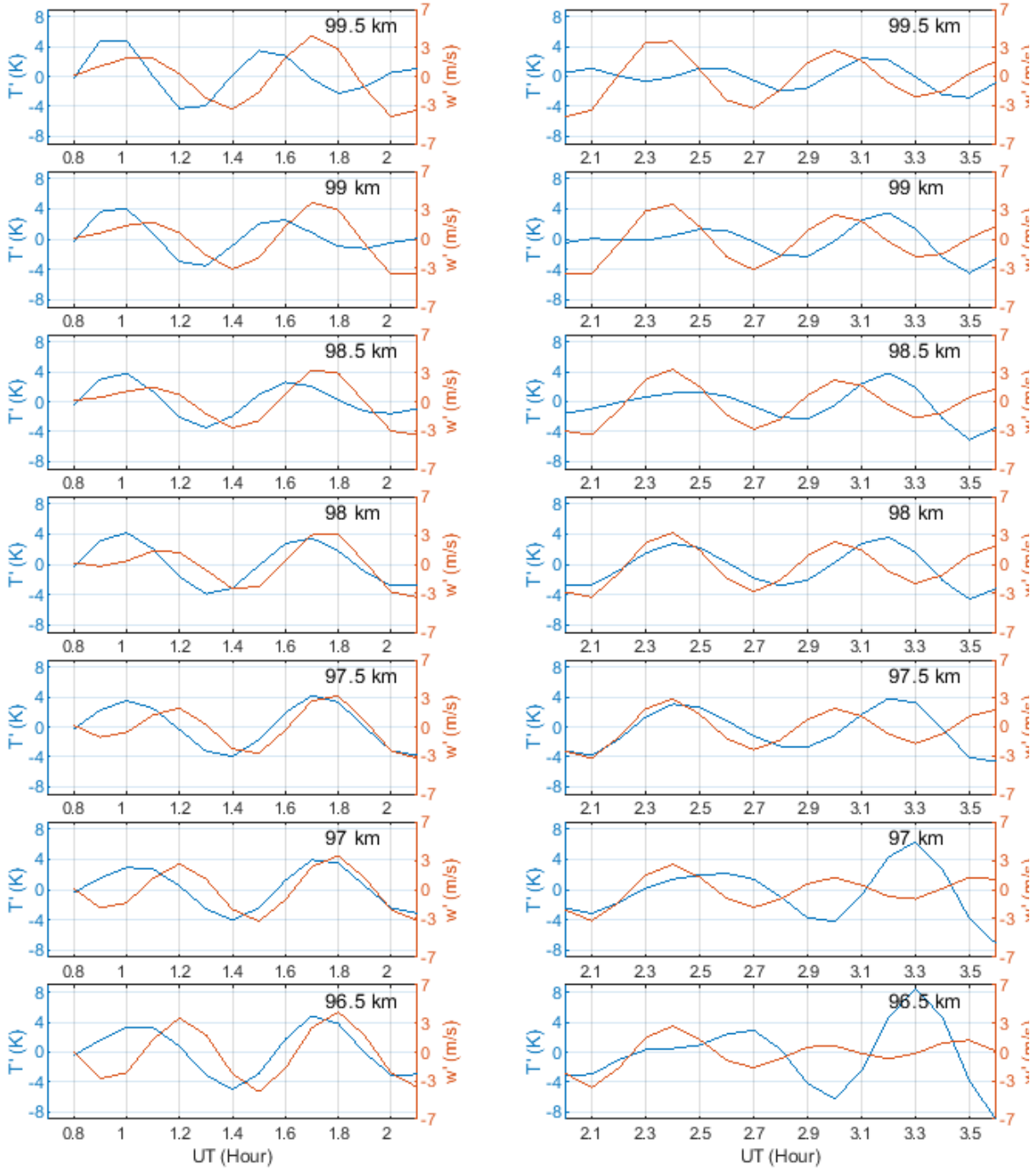

Figure A.2 Same as Figure A.1, but for the altitude range 96.5–99.5 km.

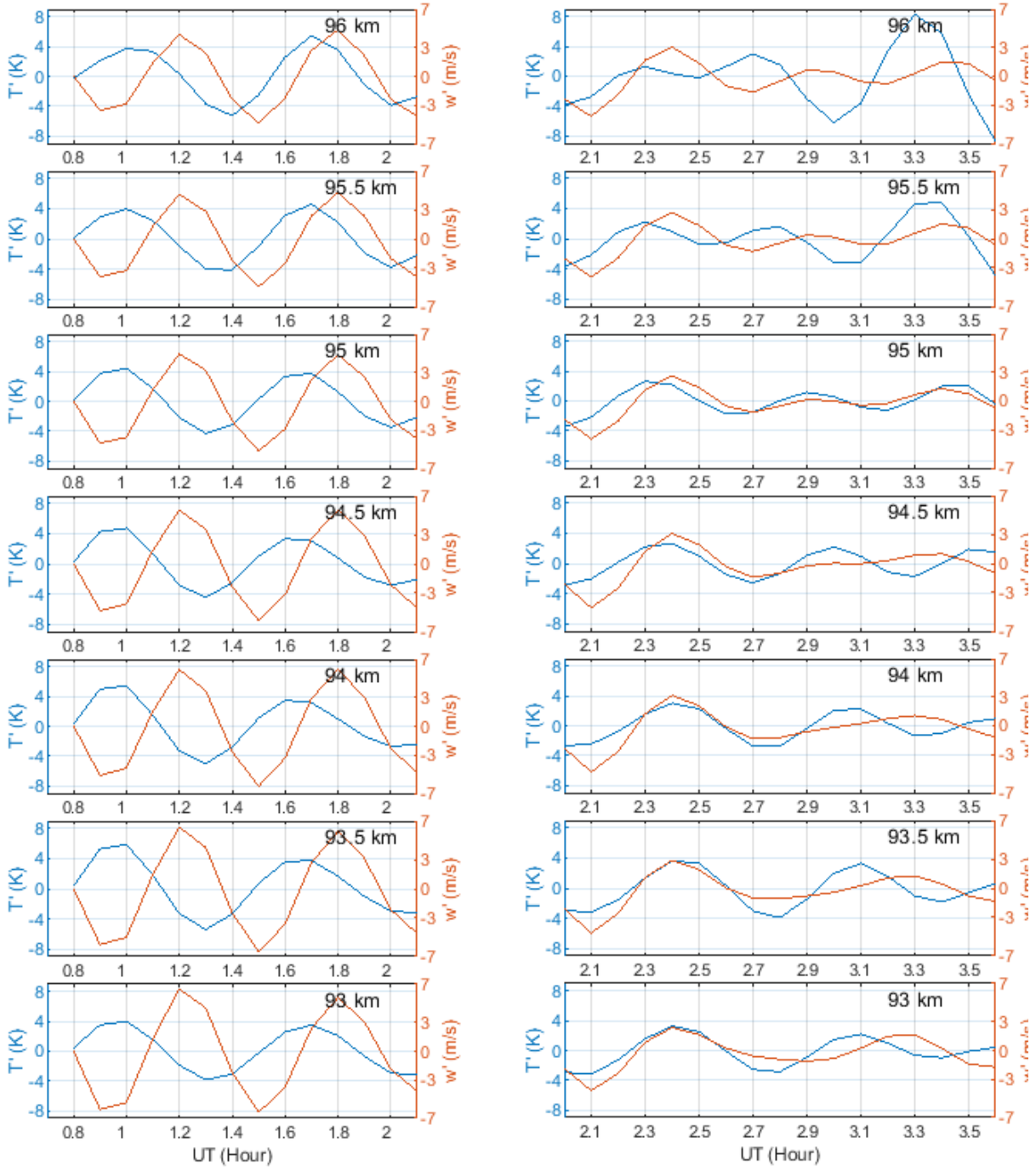

Figure A.3 Same as Figure A.1, but for the altitude range 93–96 km.

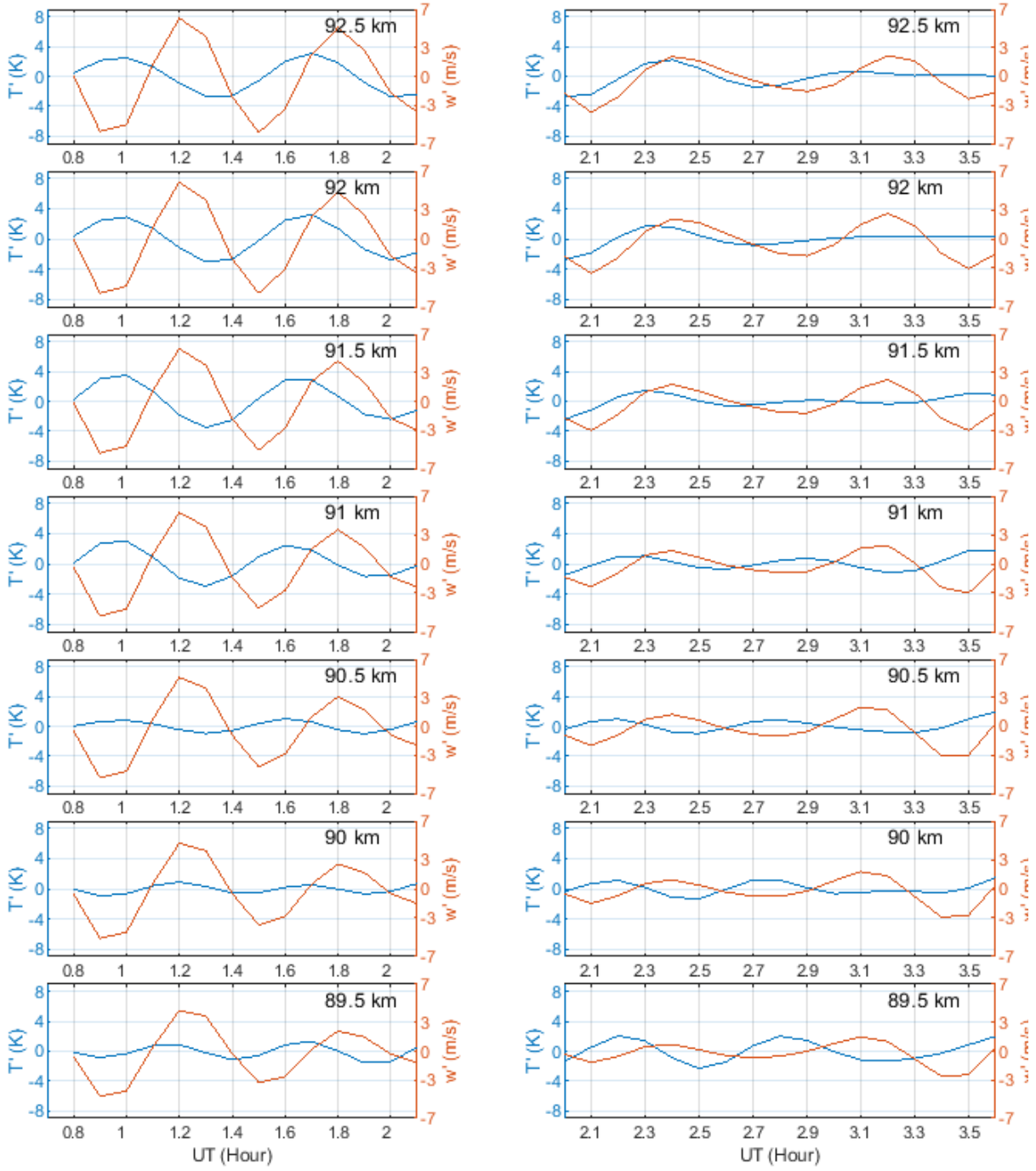

Figure A.4 Same as Figure A.1, but for the altitude range 89.5–92.5 km.

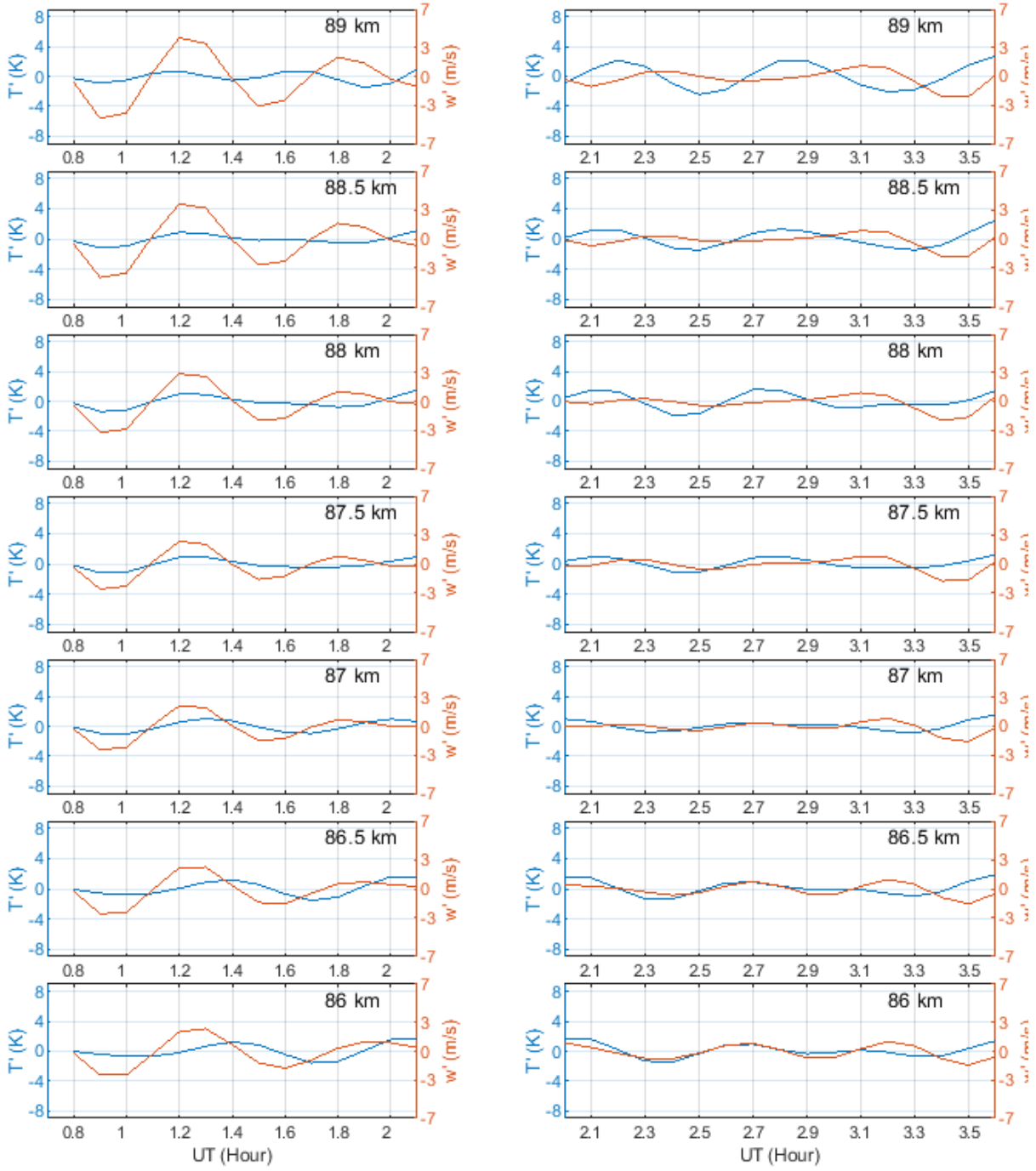

Figure A.5 Same as Figure A.1, but for the altitude range 86–89 km.

Appendix B: Linearization of the Incompressible Euler Equations

The linearization of the Euler equations for the set of fundamental variables *q* defined in Equation (1.1) is developed following Cao [2017]. The atmosphere is assumed to be inviscid, irrotational (i.e., ignoring the effects of Earth's rotation), and, initially, compressible. The atmosphere is also assumed to have vertical variations in the background temperature and winds, but without variation in the horizontal plane. We first consider a 2-D reference plane in the horizontal (*x*) and vertical (*z*) directions. For a 2-D wind vector $\vec{U} = (u, w)$, the material derivative operator is given by

$$\frac{d}{dt} = \frac{\partial}{\partial t} + \vec{U} \cdot \nabla, \tag{B.1}$$

where $\frac{\partial}{\partial t}$ is the local derivative relative to a fixed point and $\vec{U} \cdot \nabla$ is the convective derivative. The corresponding Euler continuity equations for the momentum, thermal energy, and mass are given by [Cao, 2017]

$$\begin{gathered} \frac{\partial \vec{U}}{\partial t} + \vec{U} \cdot \nabla \vec{U} = -\frac{1}{\rho} \nabla p + \vec{\mathrm{g}} \\ \frac{\partial p}{\partial t} + \vec{U} \cdot \nabla p = c_s^2 \left(\frac{\partial \rho}{\partial t} + \vec{U} \cdot \nabla \rho \right) \\ \frac{\partial \rho}{\partial t} + \nabla \cdot \left(\rho \vec{U} \right) = 0, \end{gathered} \tag{B.2}$$

where ρ is the atmospheric density, p is the atmospheric pressure, $\vec{\mathrm{g}}$ is the gravitational acceleration vector due to Earth's gravitational field, and c_s is the speed of sound in the atmosphere. In the limit where the Boussinesq approximation that the pressure and density changes are separable is valid, we consider only the density perturbations which occur along with the gravitational acceleration *g*. Consequently, the atmosphere is now assumed to be incompressible. The Euler equations (B.2) become

$$\begin{aligned} \frac{\partial \vec{U}}{\partial t} + \vec{U} \cdot \nabla \vec{U} &= -\frac{1}{\bar{\rho}} \nabla p + \vec{\mathrm{g}} \\ \frac{\partial \rho}{\partial t} + \vec{U} \cdot \nabla \rho &= 0 \\ \nabla \cdot \vec{U} &= 0, \end{aligned} \tag{B.3}$$

which are the Taylor-Goldstein equations. Using the 2-D reference plane, we may write the scalar forms of Equations (B.3) as

$$\begin{aligned} \frac{\partial u}{\partial t} + u\frac{\partial u}{\partial x} + w\frac{\partial u}{\partial z} &= -\frac{1}{\rho}\frac{\partial p}{\partial x} \\ \frac{\partial w}{\partial t} + u\frac{\partial w}{\partial x} + w\frac{\partial w}{\partial z} &= -\frac{1}{\rho}\frac{\partial p}{\partial z} - g \\ \frac{\partial u}{\partial x} + \frac{\partial w}{\partial z} &= 0 \\ \frac{\partial \rho}{\partial t} + u\frac{\partial \rho}{\partial x} + w\frac{\partial \rho}{\partial z} &= 0. \end{aligned} \tag{B.4}$$

We now expand each variable in the set q into the sum of a slowly varying background state $\bar{q}$, which depends only on the altitude, and a small first-order perturbation q' as

$$q(x, z, t) = \bar{q}(z) + q'(x, z, t). \tag{B.5}$$

Equation (B.4) then becomes

$$\begin{aligned} \frac{\partial u'}{\partial t} + \bar{u}\frac{\partial u'}{\partial x} + w'\frac{d\bar{u}}{dz} &= -\frac{1}{\bar{\rho}}\frac{\partial p'}{\partial x} \\ \frac{\partial w'}{\partial t} + \bar{u}\frac{\partial w'}{\partial x} &= -\frac{1}{\bar{\rho}}\frac{\partial p'}{\partial z} - \frac{\rho'}{\bar{\rho}}g \\ \frac{\partial u'}{\partial x} + \frac{\partial w'}{\partial z} &= 0 \\ \frac{\partial \rho'}{\partial t} + \bar{u}\frac{\partial \rho'}{\partial x} + w'\frac{d\bar{\rho}}{dz} &= 0. \end{aligned} \tag{B.6}$$

We now assume waveform solutions of the form

$$q'(x, z, t) = \tilde{q}(z)e^{i(kx - \omega \mathrm{t})}, \tag{B.7}$$

where k is the horizontal wavenumber and ω is the extrinsic angular frequency. Equation (B.6) becomes

$$
\begin{aligned}
-i\omega\tilde{u} + i\bar{u}k\tilde{u} + \tilde{w}\frac{d\bar{u}}{dz} &= -\frac{i}{\bar{\rho}}k\tilde{\rho} \\
-i\omega\tilde{w} + i\bar{u}k\tilde{w} &= -\frac{1}{\bar{\rho}}\frac{d\tilde{p}}{dz} - \frac{\tilde{\rho}}{\bar{\rho}}g \\
ik\tilde{u} + \frac{d\tilde{w}}{dz} &= 0 \\
-iw\tilde{\rho} + \mathrm{i}\bar{u}k\tilde{\rho} + \tilde{w}\frac{\partial\bar{\rho}}{\partial z} &= 0.
\end{aligned}
\tag{B.8}
$$

We now define the intrinsic angular wave frequency $\hat{\omega}$, or the frequency of the wave in a reference frame moving at the speed of the mean background flow $\bar{u}$, as

$$
\hat{\omega} = \omega - \bar{u}k. \tag{B.9}
$$

We also define the potential temperature θ, or the temperature (*T*) change which a parcel of fluid would undergo in an adiabatic shift from its pressure *p* to a standard reference pressure p_0, as

$$
\theta = T\left(\frac{p_0}{p}\right)^{\frac{R}{c_p}} = \frac{p}{\rho R}\left(\frac{p_0}{p}\right)^{\frac{R}{c_p}} \tag{B.10}
$$

such that the buoyancy frequency N^2 can be written as

$$
N^2 = \frac{g}{\bar{\theta}}\frac{\partial\bar{\theta}}{\partial z} = -\frac{g}{\bar{\rho}}\frac{\partial\bar{\rho}}{\partial z}. \tag{B.11}
$$

In an atmosphere with horizontally uniform temperature, the vertical variation in the atmospheric density is

$$
\bar{\rho} = \rho_0 e^{-\frac{z}{H_s}}, \tag{B.12}
$$

where ρ_0 is the ground-level atmospheric density. The solution for $\tilde{w}$ in Equation (B.8) is

$$
\frac{d^2\tilde{w}}{dz^2} - \frac{1}{H_s}\frac{d\tilde{w}}{dz} + \left(\frac{k^2N^2}{\hat{\omega}^2} + \frac{k}{\hat{\omega}}\frac{d^2\bar{u}}{dz^2} - \frac{k}{\hat{\omega}H_s}\frac{d\bar{u}}{dz} - k^2\right)\tilde{w} = 0, \tag{B.13}
$$

where we have used the definitions in Equations (B.9), (B.11), and (B.12) to simplify the result. We may also define a new variable $\hat{q}$ as

$$\hat{q} = e^{-\left(\frac{z}{2H_s}\right)}\tilde{q}. \tag{B.14}$$

Using the definition of the extrinsic horizontal phase speed *c*, we have

$$c = \frac{\omega}{k} = \frac{\hat{\omega} + k\bar{u}}{k} = \frac{\hat{\omega}}{k} + \bar{u}, \tag{B.15}$$

which can be rearranged as

$$c - \bar{u} = \frac{\hat{\omega}}{k}, \tag{B.16}$$

where the quantity $c - \bar{u}$ is the intrinsic horizontal phase speed of the wave. Using Equations (B.14) and (B.16), we may finally rewrite the Taylor-Goldstein equation in the form

$$\frac{d^2\hat{w}}{dz^2} + \left(\frac{N^2}{(c-\bar{u})^2} - k^2 - \frac{1}{4H_s^2} + \frac{1}{(c-\bar{u})}\frac{d^2\bar{u}}{dz^2} - \frac{1}{H_s(c-\bar{u})}\frac{d\bar{u}}{dz}\right)\hat{w} = 0, \tag{B.15}$$

which implies the relation in Equation (1.3).